IFN-γ signaling is required for the efficient replication of murine hepatitis virus (MHV) strain JHM in the brains of infected mice.

Catherine M. Kerr, Macie A. Proctor-Roser, Srivatsan Parthasarathy, Joseph J. O'Connor, Jessica J. Pfannenstiel, Robin C. Orozco[#], Anthony R. Fehr[#]

Department of Molecular Biosciences, University of Kansas, Lawrence, Kansas, USA

[#]Correspondance: arfehr@ku.edu; orozco.robin@ku.edu

Running title: IFN-γ is required for MHV-JHM replication in the brain

Keywords: murine hepatitis virus (MHV), coronavirus, interferon-beta (IFN-β), interferon-gamma (IFN-γ), macrodomain, PARPs, microglia, encephalitis

15 **ABSTRACT**

16 Neurotropic viruses are a major public health concern as they can cause encephalitis and
17 other severe brain diseases. Many of these viruses, including flaviviruses, herpesviruses,
18 rhabdoviruses and alphaviruses enter the brain through the olfactory neuroepithelium (ONE) in
19 the olfactory bulbs (OB). Due to the low percentage of encephalitis that occurs following these
20 infections, it's thought that the OBs have specialized innate immune responses to eliminate viruses.
21 Murine hepatitis virus strain JHM (JHMV) is a model coronavirus that causes severe encephalitis
22 in mice and can access the brain through olfactory sensory neurons. We've shown that a JHMV
23 Mac1-mutant virus, N1347A, has decreased replication and disease in the brains of mice. Here we
24 further show that this virus replicates poorly in the OB. However, it is unknown which innate
25 immune factors restrict N1347A replication in the OB. RNA seq analysis of infected olfactory
26 bulbs showed that IFNγ was upregulated in the OB while IFN-β was barely detectable at 5 days
27 post-infection. To determine if IFN-γ restricts JHMV N1347A replication, we utilized IFN-γ and
28 IFN-γ receptor (IFN-γR) knockout (KO) mice. Surprisingly we found that JHMV WT and N1347A
29 replicated very poorly in the OB and whole brains of both IFN-γ and IFN-γR KO mice following
30 intranasal infection, though survival and weight loss were unaltered. Furthermore, we determined
31 that microglia were the primary cells producing IFN-γ during the early stages of this infection. We
32 conclude that IFN-γ is required for the efficient replication of JHMV in the brains of infected mice.

33 **INTRODUCTION**

34 Viruses that infect the brain are a major public health threat, as they can lead to severe
35 disease such as encephalitis, encephalomyelitis, flaccid paralysis, and aseptic meningitis.
36 Neurotropic viruses can enter the brain through several mechanisms, including anterograde spread
37 through sensory nerves, across the blood-brain barrier (BBB) as free virions, or through infection
38 of immune cells that then enter the brain through the BBB. However, the most common route is
39 through the olfactory bulb (OB) [1, 2]. Viruses that utilize OBs as an entrance to the central
40 nervous system (CNS) are influenza A virus, herpesviruses, poliovirus, rabies virus, adenoviruses,
41 Japanese encephalitis virus, West Nile virus, chikungunya virus, severe acute respiratory
42 syndrome coronavirus 2 (SARS-CoV-2), and many others [2]. Importantly, SARS-CoV-2 utilizes
43 the olfactory epithelium as a major entry point to the brain which can lead to encephalopathy and
44 other neurological sequelae in some patients [3-8]. Despite the potential for severe consequences
45 of a brain infection, severe disease following infection is somewhat rare, indicating that the cells
46 in the OB have a robust innate immune response to limit virus replication and pathogenesis.
47 However, we lack a full understanding of the main factors that limit virus replication in the
48 olfactory bulb. Thus, understanding how cells in the olfactory bulb, including the olfactory neurons
49 and epithelium respond to virus infection will be critical to develop novel methods to control
50 neurotropic viruses.

51 The olfactory epithelium is adjacent to the respiratory epithelium in the upper airways
52 where olfactory sensory neurons (OSNs) detect odorants which allow mammals to detect different
53 scents. Axons of the OSNs interact with the dendrites of projection neurons in the glomeruli of the
54 OB. Projection neurons send signals deeper into the brain, which are regulated by interneurons of
55 the OB. Neurotropic strains of murine CoVs, specifically mouse hepatitis virus (MHV) strain JHM

56 (JHMV) and its attenuated variant J2.2, cause acute encephalitis and CNS demyelination,
57 respectively [9]. These viruses directly infect OSNs and enter the OB through anterograde
58 transport via the olfactory nerve. JHMV then spreads *trans*-neuronally to connections of the OB
59 which then allows it to traverse through the brain, ultimately leading to severe encephalitis or CNS
60 demyelination [10, 11].

61 Coronavirus (CoVs) are positive-sense RNA viruses with a large genome of around 30kb.
62 They have sixteen non-structural proteins (nsps) that are important for virus replication. The
63 largest of these proteins is nsp3, which contains several domains, including ubiquitin-like domains,
64 one or two papain-like protease domains, a deubiquitinase domain, a CoV-Y domain, and one or
65 more macrodomains [12]. Of these macrodomains, the most N-terminal macrodomain, termed
66 Mac1, is a conserved throughout the *Coronaviridae* family, and is also found in the *Togaviriadae,*
67 *Hepeviridae*, and *Matonaviridae* families [13, 14]. Mac1 acts as an ADP-ribosylhydrolase, which
68 removes ADP-ribose from target proteins [15]. We and others have used reverse genetics to define
69 the role of Mac1 during CoV infection [16-26]. The primary Mac1 modification used in these
70 studies is the mutation of a highly conserved asparagine to alanine (N-A), which is known to ablate
71 the enzymatic activity of this protein [21, 25, 27]. These studies have found that recombinant
72 viruses with this mutation replicate poorly and cause minimal disease in mice [18, 20, 21, 26, 27].
73 Specifically, the JHMV N1347A mutant virus replicates normally in standard cell lines used for
74 JHMV but is highly attenuated in primary bone-marrow derived macrophages (BMDMs) and in
75 mice [20, 28, 29]. Importantly, this attenuation is mediated at least in part by IFN-I, as N1347A
76 replication and pathogenesis was mostly rescued in IFNAR$^{-/-}$ cells and mice [28]. In addition,
77 JHMV N1347A was more sensitive to pre-treatment of BMDMs with IFN-β than WT virus.
78 Finally, microglia were critical for the restriction of N1347A in mice, as mice depleted of microglia

79 were highly sensitive to N1347A, unlike mice with intact microglia, indicating that microglia are
80 the likely producers of IFN-I during JHMV infection [11].

81 ADP-ribosylation is a common post-translational modification of target proteins. It is
82 catalyzed by ADP-ribosyltransferases, the most common of which are PARPs, which can add
83 either a single ADP-ribose moiety (MARylation) or a chain of moieties (PARylation) [30]. Several
84 PARPs are also interferon stimulating genes (ISGs), as they are unregulated upon IFN stimulation
85 [28, 31, 32]. As such, a number of PARPs have antiviral activity [33-40]. Previously, using pan-
86 PARP inhibitors we demonstrated that PARPs inhibit JHMV replication in the absence of Mac1
87 activity [28]. More recently, we showed that PARP12, an ISG, is required to for the restriction of
88 N1347A replication in cell culture and *in vivo* in a cell and tissue specific manner [41]. JHMV
89 N1347A replication was increased to WT virus levels in PARP12$^{-/-}$ BMDMs. However, in mice
90 the absence of PARP12 resulted in several different levels of virus restoration depending on the
91 tissue and route of infection. MHV-A59 N1348A (same mutation as in JHMV) replication was
92 increased to WT levels in the livers of PARP12$^{-/-}$ mice compared to PARP12$^{+/+}$ mice and the
93 pathology in the liver was partially restored. Following an intracranial infection of PARP12$^{-/-}$ mice,
94 JHMV N1347A replication and lethality was increased compared to PARP12$^{+/+}$ mice but not to
95 WT virus levels. Finally, we found no difference in N1347A replication or virulence following an
96 intranasal infection, which enters the brain through OSNs, of PARP12$^{-/-}$ mice compared to WT
97 mice [41]. This indicates that PARPs, specifically PARP12, are involved in restricting Mac1
98 mutant virus replication *in vivo* but that there must be additional immune factors in the OBs that
99 control N1347A replication and its disease outcomes.

100 In this study, we aimed to identify host innate immune factors, specifically PARPs, that
101 might restrict N1347A in the OBs of mice. We found that IFN-γ, but not IFN-I, was highly

102 upregulated in OBs early after infection, but surprisingly found that, unlike IFN-I, IFN-γ was
103 required for the efficient replication of JHMV in mice, as JHMV WT and N1347A replication was
104 dramatically reduced in IFN-$\gamma^{-/-}$ and IFN-γR$^{-/-}$ mice. These results provide new insight into the
105 impact of IFN-γ on the replication of a neurotropic CoV.

106 **RESULTS**

107 *JHMV-N1347A replicates poorly in the olfactory bulbs following intranasal infection.*

108 We recently demonstrated that JHMV N1347A replication is increased following an
109 intracranial infection of PARP12$^{-/-}$ mice compared to WT mice, but not following an intranasal
110 infection [41]. Therefore, we tested the ability of N1347A to replicate at the initial site of an
111 intranasal infection, the OBs. WT (+/+) mice were infected with either the WT virus or N1347A
112 virus, then OBs were harvested at peak titer (5 days post-infection (dpi)) to determine the levels
113 of virus replication. We could not identify significant levels of infectious virus prior to this time
114 point in the olfactory bulb (data not shown). We found that levels of N1347A infectious virus and
115 genomic RNA levels were significantly reduced compared to the WT virus in the OB **(Fig. 1A-B)**.
116 Additionally, less N protein was observed by immunohistochemistry in N1347A infected olfactory
117 bulbs compared to WT infected olfactory bulbs **(Fig. 1C)**. Taken together, this data indicates that
118 N1347A replicates poorly in the OB and is likely restricted by one or more unknown host factors.

119 *IFN-γ is upregulated in infected olfactory bulbs.*

120 Next, we utilized RNAseq to identify immune factors in the olfactory bulb that could be
121 responsible for the observed reduction in N1347A replication. Interestingly, compared to naïve
122 mice, we observed that IFN-II, or IFN-γ, but not IFN-I, was upregulated in the olfactory bulb upon
123 an N1347A infection **(Fig. 2A-B and Table S1)**. In addition to IFN-γ, several other ISGs were
124 upregulated as well, including ISG15, ISG20, CXCL9, CXCL10, CXCL11, IFIT2, IFIT3, RSAD1,

125 RSAD2, and several PARPs **(Fig. 2A-B)**. We then used qPCR to confirm that IFN-γ, but not
126 IFNβ, was upregulated in the OBs following JHMV infection **(Fig. 2C)**. We've recently shown
127 that pre-treatment of cells with IFN-γ in cell culture induces PARP expression [18], so despite the
128 lack of IFN-I, we analyzed the OBs for PARP expression. We identified 7 PARPs that were
129 upregulated in OBs following JHMV infection, including PARP3, 7, 9, 11, 12, 13, and 14 **(Fig.**
130 **2D)**, one or more of which likely contribute to the repression of N1347A in OBs.

131 *IFN-γ is required for efficient replication of JHMV in the brain.*

132 Because we previously demonstrated that IFN-γ leads to upregulation of PARPs, we
133 hypothesized that in the absence of IFN-γ or IFN-γ signaling JHMV N1347A replication and
134 pathogenesis would be enhanced. However, what we observed was quite the opposite. At 5 dpi,
135 JHMV WT viral loads were significantly reduced in both IFN-$\gamma^{-/-}$ and IFN-$\gamma R^{-/-}$ OBs, and N1347A
136 viral loads were extremely low in all mice, clearly demonstrating that deletion of IFN-γ or IFN-γ
137 signaling did not enhance JHMV N1347A replication in the OBs **(Fig. 3A)**. We next analyzed
138 viral loads in the whole brains of these mice at 5 dpi and found that both JHMV WT and N1347A
139 viral loads were significantly decreased in IFN-$\gamma^{-/-}$ and IFN-$\gamma R^{-/-}$ mice **(Fig. 3B)**. This indicates
140 that IFN-γ may be required for efficient JHMV replication following intranasal inoculation. To
141 test this hypothesis using a separate measure of virus replication, we measured viral genomic and
142 sub-genomic RNA of WT virus in the olfactory bulbs **(Fig. 3C)** and whole brains **(Fig. 3D)** of
143 WT, IFN-$\gamma^{-/-}$, and IFN-$\gamma R^{-/-}$ mice. In most cases, viral RNA levels were reduced in IFN-$\gamma^{-/-}$, and
144 IFN-$\gamma R^{-/-}$ mice, with statistically significant reduction of viral RNA in the whole brains. To further
145 demonstrate that viral replication is repressed in the olfactory bulb, we stained infected WT and
146 IFN-$\gamma^{-/-}$ olfactory bulbs for the CoV N protein using immunohistochemistry to identify cells with
147 actively replicating virus. JHMV WT infected OBs from WT mice had robust N protein staining,

148 while N1347A staining was reduced compared to WT virus **(Fig. 3E-F)**. However, the expression
149 of N protein in both the OB and forebrain of IFN-$\gamma^{-/-}$ mice was substantially reduced compared to
150 WT mice following infection of both JHMV WT and N1347A **(Fig. 3E-F and Fig. S1)**. In
151 combination, these results indicate that IFN-γ is required for efficient replication of JHMV in the
152 brain following intranasal infection.

153 *The loss of IFN-γ or IFN-γ signaling does not impact JHMV-induced lethality.*

154 We next asked if the limited virus replication following JHMV intranasal infection in mice
155 lacking IFN-γ or IFN-γ signaling would impact viral pathogenesis. WT, IFN-$\gamma^{-/-}$, or IFN-$\gamma R^{-/-}$ mice
156 were infected with WT JHMV and monitored for weight loss and lethality. Using a dose of 1×10^4
157 PFU JHMV, we observed no difference in the lethality or weight loss in any of these mice **(Fig.**
158 **4A)**. We next tested if differences in pathogenesis might only be observed at lower doses of virus,
159 so we infected mice with both 3×10^3 and 1×10^3 PFU. Despite these lower doses, we observed no
160 consistent differences in the pathogenesis of JHMV in IFN-$\gamma^{-/-}$ or IFN-$\gamma R^{-/-}$ mice **(Fig. 4B-C)**. We
161 conclude that despite reduced levels of virus replication, the loss of IFN-γ or IFN-γ signaling does
162 not affect the ability of JHMV to cause severe disease in mice. It also suggests that virus replication
163 is not necessarily coupled to pathogenesis in the brains of mice infected with JHMV.

164 *The loss of IFN-γ or IFN-γ signaling does not impact JHMV replication in ex vivo BMDMs.*

165 To test whether JHMV replicates poorly in IFN-$\gamma^{-/-}$ or IFN-$\gamma R^{-/-}$ cells *ex vivo*, we harvested
166 bone marrow from IFN-$\gamma^{-/-}$ or IFN-$\gamma R^{-/-}$ mice and differentiated them into bone-marrow derived
167 macrophages (BMDMs), which are susceptible to JHMV. BMDMs were infected at an MOI of 0.1
168 and harvested at 20 hpi and infectious virus and viral RNA were measured by plaque assay and
169 qPCR, respectively. There were no significant differences in the production of infectious virus or
170 viral RNA following JHMV WT or N1347A virus infection IFN-$\gamma^{-/-}$ or IFN-$\gamma R^{-/-}$ cells when

171 compared to WT cells **(Fig. 5A and Fig. S2)**. Of note, we have previously found that BMDMs
172 produce very little IFN-γ (data not shown). These results indicates that cells lacking IFN-γ do not
173 have an intrinsic defect in virus replication. Next, we pre-treated BMDMs with recombinant IFN-γ
174 to test its ability to directly affect virus replication. The exogenous addition of IFN-γ to BMDMs
175 reduced virus replication **(Fig. 5B)**. These results demonstrate that IFN-γ does not directly enhance
176 virus replication and that the effects observed in the brain following intranasal infection are likely
177 indirect effects of IFN-γ on cells in the brain.

178 *The loss of IFN-γ signaling does not impact cytokine production or the immune cell profile of*
179 *JHMV-infected brains.*

180 To try to explain how IFN-γ might alter virus replication *in vivo*, we next tested whether
181 JHMV infection of IFN-$\gamma^{-/-}$ or IFN-$\gamma R^{-/-}$ mice induce increased levels of IFN-I or other cytokines
182 that could lead to reduced viral loads in the brain. To determine the levels of cytokines in the brain,
183 we harvested both the olfactory bulbs and whole brains from JHMV WT infected mice at 5 dpi,
184 prepared RNA, and measured the levels of IFN-β, IFN-γ, IL-1β, CXCL10, and IL-6 mRNA in
185 WT, IFN-$\gamma^{-/-}$ or IFN-$\gamma R^{-/-}$ mice using quantitative PCR **(Fig. 6A)**. The levels of most cytokines
186 were not statistically different between the different strains of mice, except for CXCL-10, which
187 was reduced in IFN-$\gamma^{-/-}$ or IFN-$\gamma R^{-/-}$ mice. This is likely due to either the lower levels of virus
188 replication or the lack of IFN-γ signaling, which is known to induce CXCL-10 **(Fig. 3C-D)**. We
189 conclude that the lack of IFN-γ signaling does not result in broad changes in cytokine production
190 following JHMV infection.

191 Next, we analyzed the immune cell profile in JHMV infected WT and IFN-$\gamma R^{-/-}$ mice by
192 flow cytometry using naïve WT mice as controls. Again, we harvested the brains of infected mice
193 at 5 dpi and measured the frequency of several innate and adaptive immune cells including

194 microglia, dendritic cells (DCs), macrophages, natural killer cells (NK), neutrophils, B cells, and
195 CD4+/CD8+ T cells **(Fig. 6B)**. We found no significant difference in any cell type between WT
196 and IFN-γR$^{-/-}$ infected mice.

197 *Microglia, CD4+ T cells, and Macrophages produce the highest amount of IFN-γ during JHMV*
198 *infection.*

199 Following JHMV intranasal infection, we observed a stark increase in IFN-γ at 5 dpi **(Fig.**
200 **2)**, which prompted us to ask which cells were producing IFN-γ in these mice following infection
201 and if the lack of IFN-γ receptor signaling impacts IFN-γ production. IFN-γ is typically produced
202 by T cells or NK cells, however, this does not preclude other cells from producing IFN-γ during
203 JHMV infection. To identify which cells produce IFN-γ, we harvested whole brains of JHMV
204 infected WT and IFN-γR$^{-/-}$ mice and measured IFN-γ production using intracellular flow
205 cytometry. During JHMV infection in WT mice, there were no statistically significant differences
206 detected between the frequency of IFN-γ + cell types, though microglia was the only cell type to
207 produce IFN-γ in each mouse that was infected (**Figure 7A)**. However, in IFN-γR$^{-/-}$ mice, there
208 were significantly more IFN-γ + NK cells, though this difference was largely driven by two outliers
209 **(Figure 7A)**. Using gMFI, microglia, CD4 T cells, and macrophages had the highest expression
210 of IFN-γ in both infected WT and IFN-γR$^{-/-}$ mice, while CD8+ T cells, NKs, and DCs produced
211 substantially less IFN-γ **(Figure 7B)**. Furthermore, the MFI levels were nearly the same between
212 the WT and IFN-γR$^{-/-}$ mice indicating that IFN-γ receptor signaling does not alter IFN-γ production
213 during JHMV infection. We conclude that microglia, CD4+ T cells, and macrophages contribute
214 to the overall production of IFN-γ following an intranasal infection with JHMV.

215 **DISCUSSION**

216 In this study, we explored the role of IFN-γ in an intranasal infection of MHV-JHM, or
217 JHMV. Our previous studies found that in WT mice a Mac1 mutant, N1347A, had a severe
218 replication defect and caused minimal disease following i.n. infection of the brain [20, 28]. While
219 Mac1-mutant virus had enhanced replication and led to increased disease in PARP12$^{-/-}$ mice
220 following both i.c. and i.p. infections, Mac1-mutant replication or disease was not enhanced at all
221 in PARP12$^{-/-}$ mice following an i.n. infection [41]. Unlike an i.c. infection, the olfactory bulb is
222 the initial site infected following i.n. injection [10]. Thus, we hypothesized that there must be
223 another PARP or innate immune factor present in the olfactory bulbs that restricts the replication
224 of N1347A. Using RNA seq, we showed that IFN-γ, but ironically not IFN-I, was upregulated in
225 the olfactory bulbs of mice following JHMV infection.

226 IFN-γ is the only known type II interferon. It is a component of both the innate and adaptive
227 immune responses and is primarily produced by activated natural killer (NK) cells, CD4^{+} T helper-
228 1 cells (T_H1), and CD8^{+} cytotoxic T cells [42]. Specific functions of IFN-γ include T-cell
229 activation, DC maturation, and polarization of macrophages to the M1 phenotype [43]. IFN-γ also
230 has antiviral properties. For example, during a herpes simplex virus 2 (HSV-2) infection, the
231 absence of IFN-γ increased virus replication and decreased survival of infected mice [44]. IFN-γ
232 has also been shown to have a protective effect in mice against a challenge of influenza A virus
233 (H1N1) [45]. This study found that WT mice were able to clear a viral challenge of H1N1
234 following an immunization with H3N2, while IFN-γ$^{-/-}$ mice were not. The increased viral loads of
235 H1N1 in IFN-γ$^{-/-}$ mice indicate the importance of IFN-γ to clear subsequent virus infections [45].
236 It was recently shown that the administration of IFN-γ prior to infection provides protection to
237 mice from a SARS-CoV-2 infection, and also suggested that the presence of IFN-γ likely decreases

238 viral load [46]. The authors hypothesized that after a first infection, the memory T cells provide
239 IFN-γ quickly following an additional exposure to another pathogen, similar to the study done with
240 the H1N1 virus [46]. Additionally, IFN-γ mRNA was found to be upregulated during both JHMV
241 and J2.2 infections [47]. It was shown to be essential for clearance of an attenuated strain of JHMV,
242 J2.2, that leads to a persistent infection, in oligodendrocytes however, in the same study, it had
243 little to no effect on viral clearance from neurons. This indicates a cell-specific role for IFN-γ
244 immunity, which may affect the outcome of disease in the IFN-γ knockout mice [48].

245 Following our RNAseq experiments, we hypothesized that the increased IFN-γ was
246 responsible for the restriction of MHV N1347A in the OB. This was largely based on a couple of
247 pieces of evidence from previous work. First, we found that the KO of IFN-I signaling increases
248 the replication of N1347A in BMDMs to near WT levels and also increased its pathogenesis.
249 However, we did not detect much, if any, IFN-I in the OBs following JHMV infection. More
250 recently we demonstrated that IFNγ pre-treatment induces PARP expression and has increased
251 antiviral activity against a Mac1-deleted SARS-CoV-2 compared to WT virus [18]. In fact, several
252 PARPs have been shown to be induced by both IFN-I and IFN-γ [49]. Thus, we hypothesized that
253 in the absence of IFN-I, the production of IFN-γ would be responsible for increased PARP and
254 ISG expression in the OB. However, we were surprised to find that the knockout of IFN-γ signaling
255 did not enhance N1347A replication, but instead reduced the replication of both WT and N1347A
256 viruses. It remains unclear what innate immune factors restrict N1347A in the OB, though one
257 primary candidate is PARP14. PARP14 was one of the PARPs that was upregulated in the OB
258 (Fig. 2D), and we have demonstrated that the knockout of PARP14 enhances N1347A replication
259 in BMDMs [50]. However, PARP14 expression is not very robust in the OB, and thus other factors
260 may play a role.

261 The more perplexing question is why is IFN-γ required for efficient JHMV replication in
262 mice following intranasal infection **(Fig. 3)**? The addition of recombinant IFN-γ to BMDMs
263 restricts virus replication **(Fig. 5C)**, and thus the requirement for IFNγ for JHMV replication during
264 i.n. infection is likely due to the impact of IFN-γ on other cells in the brain. There was no significant
265 difference in the levels of immune cells in WT vs IFN-γR$^{-/-}$ mice, suggesting that IFN-γ may be
266 more likely to impact non-hematopoetic cells in the brain that are susceptible to infection. IFN-γ
267 is important for neuronal cell development [51], and the differentiation of neuronal precursor cells
268 through cross talk with sonic hedgehog signaling [52]. Thus, it is possible that the lack of IFN-γ
269 signaling from birth may impact olfactory neurons or other cells in the brain, such as astrocytes,
270 that makes them less permissive to JHMV infection. It remains unclear what specific impacts IFN-
271 γ has on cells in the OB that promote JHMV replication.

272 Finally, we were interested in the source of the IFN-γ that we observed at 5 dpi with JHMV.
273 IFN-γ is primarily produced by CD8+ T cells and NK cells. However, other immune cells, such
274 antigen-presenting cells, can produce IFN-γ as well. To determine which cell types were the
275 predominant contributors of IFN-γ in the brain during JHMV infection, we quantified the
276 percentage of immune cells expressing IFN-γ and the amount of IFN-γ production by different
277 immune cells in the brains of infected animals using flow cytometry. Our results indicate that
278 microglia constitute a significant proportion of immune cells in the brain **(Fig. 6)**. Further, the
279 expression of IFN-γ in microglia was amongst the highest of immune cell populations we looked
280 at (**Fig. 7B**)**.** NK cells and CD4+ T cells produced comparably high levels of IFN-γ during infection
281 as well (**Fig. 7B**). However, the proportion of CD4+ T cells and NK cells are less (**Fig. 6**), and in
282 several mice these cells did not produce any IFN-γ (**Fig. 7A**). Taken together, we put forward that

283 microglia are a major IFN-γ producing cell type following JHMV i.n. infection, though we can't
284 rule out contributions from T cells, NK cells, macrophages, and even non-hematopoetic cells.
285 There are only limited reports demonstrating that microglia and other brain resident cells can
286 produce IFN-γ, though evidence clearly demonstrates a role for microglia in the production of IFN-
287 γ following Toxoplasma gondii infection [53-56]. This study provides additional evidence that
288 microglia can be significant producers of IFN-γ following a virus infection in the brain. Future
289 studies will be needed to further define how IFN-γ produced by microglia might impact both
290 neuronal development and neurotropic virus infections.

291 **METHODS**

292 **Cell Culture.** HeLa cells expressing the MHV receptor carcinoembryonic antigen-related cell
293 adhesion molecule 1 (CEACAM1) (HeLa-MHVR) were grown in Dulbecco's Modified Eagle
294 Medium (DMEM) supplemented with 10% fetal bovine serum (FBS), 100 U/ml penicillin and 100
295 mg/ml streptomycin, HEPES, sodium pyruvate, non-essential amino acids, and L-glutamine. Bone
296 marrow-derived macrophages (BMDMs) sourced from WT, IFN-$\gamma^{-/-}$ or IFN-$\gamma R^{-/-}$ mice were
297 differentiated into M0 macrophages by incubating cells in Roswell Park Memorial Institute
298 (RPMI) media supplemented with M-CSF (GenScript), 10% FBS, sodium pyruvate, 100 U/ml
299 penicillin and 100 mg/ml streptomycin, and L-glutamine for six days. Then to differentiate into
300 M2 macrophages, IL-4 (Peprotech Inc.) was added for 1 day. Cells were washed and replaced with
301 fresh media every other day after the 4th day.

302 **Mice.** Pathogen-free C57BL/6 (B6) WT, IFN-γ, and IFN-γR knockout mice were originally
303 purchased from Jackson Laboratories and mice were bred and maintained in the animal care
304 facilities at the University of Kansas. Animal studies were approved by the University of Kansas
305 Institutional Animal Care and Use Committees (IACUC) (permit #s 252-01 (ARF) and 278-01
306 (RCO) following guidelines set forth in the Guide for the Care and Use of Laboratory Animals.

307 **Virus Infection.** Recombinant MHV-JHMV was previously described [20]. For intranasal
308 infections, 5-8 week-old male and female mice were anesthetized with isoflurane and inoculated
309 intranasally with 1×10^4 PFU (unless otherwise stated) recombinant JHMV in a total volume of 12
310 μl DMEM. To obtain viral titers from infected animals, mice were sacrificed, and brain tissue was
311 collected and homogenized in DMEM. Viral titers were determined by plaque assay using HeLa-
312 MHVR cells.

313 **RNA Seq.** RNA was isolated from C57BL6 mice either mock infected or infected i.n. with 1×10^4
314 PFU N1347A virus using RNA purification columns (Qiagen). Library preparation was performed
315 by the University of Kansas Genome Sequencing core facility, using the NEB Next RNA Library
316 kit (NEB) with indexing. RNA-seq was performed using an Illumina NextSeq2000 high-output
317 system with a paired-end reads of 50 bp each. Raw reads were processed with the nf-core RNA-
318 seq pipeline v. 3.12.0 with Nextflow v. 23.04.3 [10.5281/zenodo.7998767]. Reads were trimmed
319 of adapter sequences with TrimGalore v. 0.6.7 [10.5281/zenodo.5127898], assessed for batch
320 effects and aligned to the C57BL6 mouse genome assembly version GRC m39 *Mus*
321 *musculus* genome assembly (GCF_000001635.27) with the Ensembl version 81 annotation using
322 STAR v 2.7.10a [57] and read count quantification was performed with RSEM v. 1.3.1 [58].
323 Differential gene expression between mock and N1347A infection treatments were estimated
324 using DESeq2 v. 1.40.2 [59] and $\log_2$-fold change values were adjusted with the lfcShrink function
325 specifying the apeglm method [60]. We classified those genes as differentially expressed that had
326 Benjamini–Hochberg FDR-adjusted *P*-value (P_{FDR}) < 0.01 and absolute $\log_2$ fold-change
327 values > 2.
328 **Real-time qPCR Analysis.** RNA was isolated from BMDMs using TRIzol (Invitrogen) and
329 cDNA was prepared using MMLV-reverse transcriptase as per manufacturer's instructions
330 (Thermo Fisher Scientific). Quantitative real-time PCR (qRT-PCR) was performed on a
331 QuantStudio3 real-time PCR system using PowerUp SYBR Green Master Mix (Thermo Fisher
332 Scientific). Primers used for qPCR are listed in Table S2. Cycle threshold (C_T) values were
333 normalized to the housekeeping gene hypoxanthine phosphoribosyltransferase (HPRT) by the
334 following equation: $C_T = C_{T(\text{gene of interest})} - C_{T(\text{HPRT})}$. Results are shown as a ratio to HPRT calculated
335 as $2^{-\Delta CT}$.

336 **Immunohistochemistry (IHC).** At 5 dpi, mice were perfused intracardially with 4%
337 formaldehyde (FA) diluted in 1X HBSS. After perfusion, each mouse brain was dissected and
338 immersed in fresh 4% FA in individual tubes for post-fixation. The OB and forebrain regions were
339 cut, placed on a freezing stage at -20°C and sectioned rostral-to-caudal at 30 µm in intervals (skip
340 60 µm between sections) using a sliding block microtome (American Optical Spencer 860 with
341 Cryo-Histomat MK-2 controller). Four to six sections per group were moved individually on a 24-
342 well plate using a camel hairbrush < 1.59 mm (Electron Microscopy Sciences, Cat. No. 65575-
343 02), free-floating on HBSS/0.1% sucrose (HBSS/Su) at room temperature (RT) for rinsing. To
344 perform single IHC, forebrain sections were permeabilized with HBSS/Su + 0.1% saponin
345 (HBSS/Su/Sap; 2x, 5 min each), blocked with HBSS/Su/Sap + 0.1% Triton X-100 + 3% rabbit
346 serum (1x, 1hr at RT), rinsed and incubated with the primary antibody mouse anti-N (1:5000)
347 diluted in HBSS/Su/Sap + 3% rabbit serum O/N at 4 °C. The next day, sections were rinsed with
348 HBSS/Su/Sap (3x, 5 min each) and incubated with the secondary antibody Alexa Fluor 594 rabbit
349 anti-mouse (1:200) diluted in HBSS/Su/Sap (3 hrs at RT), rinsed with HBSS/Su/Sap (2x, 5 min
350 each), HBSS/Su (1x, 5 min) and HBSS (1x, 5 min). Then Neurotrace™ (1:25) and DAPI (10 µM)
351 diluted in HBSS were added to stain for neurons and nuclear counterstain, respectively (1hr at
352 RT), and then rinsed with HBSS (2x, 5 min each). Sections were carefully moved on a microscope
353 slide using a camel hairbrush < 1.59 mm, mounted with Vectashield® Antifade mounting medium,
354 and cover-slipped (22 x 50 cover glass; No. 1.5 thickness) for imaging.
355 **Image Acquisition and Quantification.** Fluorescent images were acquired using a TCS SPE
356 Laser Scanning Confocal Upright Microscope (Leica Microsystems, DM6-Q model), with the 405
357 nm and 561 nm laser lines, an Olympus 20X/0.75NA UPlanSApo infinity corrected, 8-bit spectral
358 PMT detector and a Leica LAS X Imaging software (version 3.5.7.23225). Two to four images

359 were taken per section. Anti-N + Alexa Fluor 594 signal was detected using 561 nm excitation
360 (35% laser intensity), 600-630 nm emission range, 700 V PMT gain, and 0% offset. DAPI signal
361 was detected using 405 nm excitation (6% laser intensity), 430-480 nm emission range, 680-700
362 V PMT gain, and 0% offset. Nissl signal was detected using 635 nm excitation (40% laser
363 intensity, 650-700 nm emission range, 700-725 V PMT gain and 0% offset. Images were captured
364 at 1024 x 1024-pixel resolution with a scan speed at 400, no bidirectional scanning, a zoom factor
365 at 1.0, Pinhole 1.0 AU = 75.54 µm (550 µm x 550 µm image size; 537.63 nm x 537.63 nm pixel
366 size; 2.057 µm optical section and 0.69 µm step size). Leica LAS X software_3D Viewer was used
367 for post-processing to create figure plates, while raw data was exported as .tiff for relative
368 fluorescent data analysis. In powerpoint, all images were set to 100% sharpness, 60% brightness,
369 and 0% contrast. All the workflow design, sample preparation, processing and imaging was
370 performed in the Microscopy and Analytical Imaging Resource Core Laboratory
371 (RRID:SCR_021801) at The University of Kansas.

372 Quantification of N protein staining was automated using a custom macro written in FIJI
373 (ImageJ v.1.54f). For each image, a median 3D filter was applied to single-channel Z-stacks (x=2,
374 y=2, z=2) after which maximum intensity Z-projections were generated. Regions of Interest
375 (ROIs) were generated following Medain 3D filtering (x=2, y=2, z=2) on duplicate single-channel
376 Z-stacks followed by automated thresholding via the Triangle method. Resulting binary masks
377 were applied to initial maximum Z-projections and fluorescence intensity of staining was
378 measured within ROIs on the relevant channel. The total area of each ROI was also measured, and
379 the Integrated Density (IntDen) displayed is a product of the mean fluorescence intensity and the
380 ROI area.

381 **Flow Cytometry and Antibodies.** Whole brains were excised and placed into RPMI with 10%
382 FBS. Samples were processed with the gentleMACS Octo Dissociator (Miltenyi Biotec, Bergisch
383 Gladbach, North Rhine-Westphalia, Germany) at 200 rpm without heat for 15 minutes. Following
384 processing, dissociated samples were filtered through 70 uM filter to create a single-cell
385 suspension in an ice-cold solution of 1 mL 10X PBS, 9 mL Percoll, and 10 mL RPMI. Tubes were
386 centrifuged at 7900 rcf for 30 minutes, the myelin layer and media were then aspirated off, being
387 careful not to disturb the pellet, leaving 10 mL of sample. The sample was centrifuged again at
388 1500 rcf for 10 minutes. Media was decanted and resuspended to desired concentration in RPMI
389 with 10% FBS. Single cell suspension was then counted using the Vi-CELL BLU cell viability
390 analyzer (Beckman Coulter, Brea, CA). Single cell suspensions were used for staining and flow
391 cytometric analysis.

392 All flow cytometry was completed on a spectral cytometer the Cytek Aurora with a 5-laser
393 system (405nm, 488nm, 640nm, 561nm, and 355nm). Single color antibody stain Positive and
394 Negative Compensation Beads (BioLegend, San Diego, CA) were used for unmixing. Unmixed
395 files were analyzed using FlowJo Software (BD Biosciences, San Diego, California). Antibodies
396 used in various combinations (depending on experiment) are as follows: Ghost Viability Dye (Blue
397 516, BioLegend, 1:1000 dilution), CD4 (Super Bright 780, Invitrogen Thermo Fisher Scientific,
398 1:250, clone RM4-5), CD8 (APC-H7, BD Pharmingen,1:250, clone 53-6.7), NK1.1 (Super Bright
399 436, Invitrogen Thermo Fisher Scientific; or V450, BD Pharmingen, 1:250, clone PK136),
400 CD45.R/B220 (APC-Cy5.5, Invitrogen Thermo Fisher Scientific, 1:250, Conjugate), F4/80
401 (Pacific Orange, Invitrogen Thermo Fisher Scientific, 1:250, Conjugate), CD3 (Super Bright 702,
402 Invitrogen Thermo Fisher Scientific, 1:250, clone 17A2), CD45 (PerCP, BioLegend, 1:250, clone
403 30-F11), CD11c (Pe-Cy5.5, Invitrogen Thermo Fisher Scientific, 1:250, clone N418), CD11b

404 (Super Bright 600, Invitrogen Thermo Fisher Scientific, 1:250, clone M1/70), Ly-6G (PE-eFluor
405 610, Invitrogen Thermo Fisher Scientific, 1:250, clone 1A8-Ly6g), CD19 (APC, BioLegend,
406 1:250, clone 6D5), CD44 (PE, eBioscience, 1:250, clone IM7), IFNγ (PE/Cy7, BioLegend, 1:100,
407 clone XMG1.2). All surface markers were stained in 1% PBS, at 4°C, in dark. For intracellular
408 cytokine staining of IFNγ, BD Cytofix and Permwash was used according to manufacturer's
409 instructions. If intracellular staining was being done, both surface and intracellular staining
410 occurred following an incubation at 37°C with 5% CO_2 for 4 hours with a BFA+RPMI.
411 **Statistics.** All results are expressed as means ± standard errors of the means (SEM). Specific
412 statistical tests used are indicated for each figure. P values of ≤0.05 were considered statistically
413 significant (*, p≤0.05; **, p≤0.01; ***, p≤0.001; ****, p ≤0.0001; ns, not significant).
414 **Data and materials availability.** All the RNAseq reads data are deposited in NCBI under the
415 BioProject ID PRJNA1202193 and BioSample ID SAMN45953065 and SAMN45953641 and will
416 be made public upon publication or March 31, 2025, whichever comes first. All other data will be
417 made available through FigShare upon publication.

ACKNOWLEDGEMENTS

We thank members of the Davido laboratory at KU for valuable discussion. Research reported in this publication was made possible in part by the services of the KU Genome Sequencing Core which is supported by the National Institutes of General Medical Sciences of the National Institutes of Health under award number P30GM145499, the KU microscopy and analytical imaging (MAI) facility, the KU Center for Genomics, the K-INBRE Genomic Data Science Core supported by the IDeA Program which is supported by the National Institutes of General Medical Sciences of the National Institutes of Health under award number P20GM103418, and the KU Flow Cytometry Core which is supported by the National Institutes of General Medical Sciences of the National Institutes of Health under award number P20GM113117. We thank our funding from the NIH, an NIH Graduate Training grant, the University of Kansas College of Liberal Arts and Sciences, and the University of Kansas Madison and Lila Self graduate programs.

Funding:

National Institutes of Health (NIH) grant R35GM138029 (ARF)
National Institutes of Health (NIH) grant P20GM113117 (ARF/RCO)
National Institutes of Health (NIH) grant K22AI134993 (ARF)
NIH Graduate Training at the Biology-Chemistry Interface grant T32GM132061 (CMK)
University of Kansas College of Liberal Arts and Sciences Graduate Research Fellowship (CMK)
University of Kansas Madison and Lila Self Fellowship (JJP/MAP)
University of Kansas Start-Up Funds (ARF/RCO)

The funders had no role in study design, data collection and analysis, decision to publish, or preparation of the manuscript. The content is solely the responsibility of the authors and does not necessarily represent the official views of the National Institutes of Health or the University of Kansas.

Author contributions:

Conceptualization: CMK, RCO, ARF
Data curation: CMK, MAP, SP, JJOC, RCO, ARF
Formal analysis: CMK, MAP, SP, JJOC, RCO, ARF
Funding acquisition: CMK, MAP, JJP, RCO, ARF
Methodology: CMK, MAP, SP, JJOC, JJP, RCO, ARF
Investigation: CMK, MAP, JP, JJP
Project administration: RCO, ARF
Resources: RCO, ARF
Visualization: CMK, MAP, SP, JJOC, RCO, ARF
Validation: CMK, MAP, SP, JJOC, RCO, ARF
Supervision: RCO, ARF
Writing—original draft: CMK, MAP, RCO, ARF
Writing—review & editing: CMK, MAP, SP, JJOC, JJP, RCO, ARF

A.R.F. was named as an inventor on a patent filed by the University of Kansas for a live-attenuated SARS-CoV-2 vaccine.

REFERENCES

1. Durrant DM, Ghosh S, Klein RS. The Olfactory Bulb: An Immunosensory Effector Organ during Neurotropic Viral Infections. ACS Chem Neurosci. 2016;7(4):464-9. Epub 20160408. doi: 10.1021/acschemneuro.6b00043. PubMed PMID: 27058872; PubMed Central PMCID: PMCPMC5775964.
2. van Riel D, Verdijk R, Kuiken T. The olfactory nerve: a shortcut for influenza and other viral diseases into the central nervous system. J Pathol. 2015;235(2):277-87. doi: 10.1002/path.4461. PubMed PMID: 25294743.
3. de Melo GD, Perraud V, Alvarez F, Vieites-Prado A, Kim S, Kergoat L, et al. Neuroinvasion and anosmia are independent phenomena upon infection with SARS-CoV-2 and its variants. Nat Commun. 2023;14(1):4485. Epub 20230726. doi: 10.1038/s41467-023-40228-7. PubMed PMID: 37495586; PubMed Central PMCID: PMCPMC10372078.
4. Meinhardt J, Radke J, Dittmayer C, Franz J, Thomas C, Mothes R, et al. Olfactory transmucosal SARS-CoV-2 invasion as a port of central nervous system entry in individuals with COVID-19. Nat Neurosci. 2021;24(2):168-75. Epub 20201130. doi: 10.1038/s41593-020-00758-5. PubMed PMID: 33257876.
5. Xydakis MS, Albers MW, Holbrook EH, Lyon DM, Shih RY, Frasnelli JA, et al. Post-viral effects of COVID-19 in the olfactory system and their implications. Lancet Neurol. 2021;20(9):753-61. Epub 20210730. doi: 10.1016/S1474-4422(21)00182-4. PubMed PMID: 34339626; PubMed Central PMCID: PMCPMC8324113.
6. Islam Z, Yamamoto S, Mizoue T, Oshiro Y, Inamura N, Konishi M, et al. Dyslipidemia and SARS-CoV-2 spike antibody titres after the second and third doses of the BNT162b2 vaccine among healthcare workers in Japan. Diabetes Metab Res Rev. 2023;39(3):e3606. Epub 20221229. doi: 10.1002/dmrr.3606. PubMed PMID: 36562447; PubMed Central PMCID: PMCPMC9880627.
7. Kasai M, Sakuma H, Abe Y, Kuki I, Maegaki Y, Murayama K, et al. Clinical characteristics of SARS-CoV-2-associated encephalopathy in children: Nationwide epidemiological study. J Neurol Sci. 2024;457:122867. Epub 20240103. doi: 10.1016/j.jns.2024.122867. PubMed PMID: 38199023.
8. Stein SR, Ramelli SC, Grazioli A, Chung JY, Singh M, Yinda CK, et al. SARS-CoV-2 infection and persistence in the human body and brain at autopsy. Nature. 2022;612(7941):758-63. Epub 20221214. doi: 10.1038/s41586-022-05542-y. PubMed PMID: 36517603; PubMed Central PMCID: PMCPMC9749650.
9. Weiss SR, Leibowitz JL. Coronavirus pathogenesis. Adv Virus Res. 2011;81:85-164. doi: 10.1016/B978-0-12-385885-6.00009-2. PubMed PMID: 22094080; PubMed Central PMCID: PMCPMC7149603.
10. Wheeler DL, Athmer J, Meyerholz DK, Perlman S. Murine Olfactory Bulb Interneurons Survive Infection with a Neurotropic Coronavirus. J Virol. 2017;91(22). Epub 20171027. doi: 10.1128/JVI.01099-17. PubMed PMID: 28835503; PubMed Central PMCID: PMCPMC5660484.
11. Wheeler DL, Sariol A, Meyerholz DK, Perlman S. Microglia are required for protection against lethal coronavirus encephalitis in mice. J Clin Invest. 2018;128(3):931-43. Epub 20180129. doi: 10.1172/JCI97229. PubMed PMID: 29376888; PubMed Central PMCID: PMCPMC5824854.

12. Wang Y, Grunewald M, Perlman S. Coronaviruses: An Updated Overview of Their Replication and Pathogenesis. Methods Mol Biol. 2020;2203:1-29. Epub 2020/08/25. doi: 10.1007/978-1-0716-0900-2_1. PubMed PMID: 32833200; PubMed Central PMCID: PMCPMC7682345.
13. Alhammad YMO, Fehr AR. The Viral Macrodomain Counters Host Antiviral ADP-Ribosylation. Viruses. 2020;12(4). Epub 2020/04/05. doi: 10.3390/v12040384. PubMed PMID: 32244383; PubMed Central PMCID: PMCPMC7232374.
14. Fehr AR, Jankevicius G, Ahel I, Perlman S. Viral Macrodomains: Unique Mediators of Viral Replication and Pathogenesis. Trends Microbiol. 2018;26(7):598-610. Epub 2017/12/23. doi: 10.1016/j.tim.2017.11.011. PubMed PMID: 29268982; PubMed Central PMCID: PMCPMC6003825.
15. Li C, Debing Y, Jankevicius G, Neyts J, Ahel I, Coutard B, et al. Viral Macro Domains Reverse Protein ADP-Ribosylation. J Virol. 2016;90(19):8478-86. Epub 2016/07/22. doi: 10.1128/JVI.00705-16. PubMed PMID: 27440879; PubMed Central PMCID: PMCPMC5021415.
16. Abraham R, Hauer D, McPherson RL, Utt A, Kirby IT, Cohen MS, et al. ADP-ribosyl-binding and hydrolase activities of the alphavirus nsP3 macrodomain are critical for initiation of virus replication. Proc Natl Acad Sci U S A. 2018;115(44):E10457-E66. Epub 2018/10/17. doi: 10.1073/pnas.1812130115. PubMed PMID: 30322911; PubMed Central PMCID: PMCPMC6217424.
17. Abraham R, McPherson RL, Dasovich M, Badiee M, Leung AKL, Griffin DE. Both ADP-Ribosyl-Binding and Hydrolase Activities of the Alphavirus nsP3 Macrodomain Affect Neurovirulence in Mice. mBio. 2020;11(1). Epub 2020/02/13. doi: 10.1128/mBio.03253-19. PubMed PMID: 32047134; PubMed Central PMCID: PMCPMC7018654.
18. Alhammad YM, Parthasarathy S, Ghimire R, Kerr CM, O'Connor JJ, Pfannenstiel JJ, et al. SARS-CoV-2 Mac1 is required for IFN antagonism and efficient virus replication in cell culture and in mice. Proc Natl Acad Sci U S A. 2023;120(35):e2302083120. Epub 20230822. doi: 10.1073/pnas.2302083120. PubMed PMID: 37607224; PubMed Central PMCID: PMCPMC10468617.
19. Eriksson KK, Cervantes-Barragan L, Ludewig B, Thiel V. Mouse hepatitis virus liver pathology is dependent on ADP-ribose-1"-phosphatase, a viral function conserved in the alpha-like supergroup. J Virol. 2008;82(24):12325-34. Epub 2008/10/17. doi: 10.1128/JVI.02082-08. PubMed PMID: 18922871; PubMed Central PMCID: PMCPMC2593347.
20. Fehr AR, Athmer J, Channappanavar R, Phillips JM, Meyerholz DK, Perlman S. The nsp3 macrodomain promotes virulence in mice with coronavirus-induced encephalitis. J Virol. 2015;89(3):1523-36. Epub 2014/11/28. doi: 10.1128/JVI.02596-14. PubMed PMID: 25428866; PubMed Central PMCID: PMCPMC4300739.
21. Fehr AR, Channappanavar R, Jankevicius G, Fett C, Zhao J, Athmer J, et al. The Conserved Coronavirus Macrodomain Promotes Virulence and Suppresses the Innate Immune Response during Severe Acute Respiratory Syndrome Coronavirus Infection. mBio. 2016;7(6). Epub 2016/12/15. doi: 10.1128/mBio.01721-16. PubMed PMID: 27965448; PubMed Central PMCID: PMCPMC5156301.
22. Kuri T, Eriksson KK, Putics A, Zust R, Snijder EJ, Davidson AD, et al. The ADP-ribose-1"-monophosphatase domains of severe acute respiratory syndrome coronavirus and human coronavirus 229E mediate resistance to antiviral interferon responses. J Gen Virol.

554 2011;92(Pt 8):1899-905. Epub 2011/04/29. doi: 10.1099/vir.0.031856-0. PubMed PMID:
555 21525212.
556 23. McPherson RL, Abraham R, Sreekumar E, Ong SE, Cheng SJ, Baxter VK, et al. ADP-
557 ribosylhydrolase activity of Chikungunya virus macrodomain is critical for virus replication
558 and virulence. Proc Natl Acad Sci U S A. 2017;114(7):1666-71. Epub 2017/02/02. doi:
559 10.1073/pnas.1621485114. PubMed PMID: 28143925; PubMed Central PMCID:
560 PMCPMC5321000.
561 24. Park E, Griffin DE. The nsP3 macro domain is important for Sindbis virus replication in
562 neurons and neurovirulence in mice. Virology. 2009;388(2):305-14. Epub 2009/04/28. doi:
563 10.1016/j.virol.2009.03.031. PubMed PMID: 19395054; PubMed Central PMCID:
564 PMCPMC2683903.
565 25. Putics A, Filipowicz W, Hall J, Gorbalenya AE, Ziebuhr J. ADP-ribose-1"-
566 monophosphatase: a conserved coronavirus enzyme that is dispensable for viral replication in
567 tissue culture. J Virol. 2005;79(20):12721-31. Epub 2005/09/29. doi:
568 10.1128/JVI.79.20.12721-12731.2005. PubMed PMID: 16188975; PubMed Central PMCID:
569 PMCPMC1235854.
570 26. Taha TY, Suryawanshi RK, Chen IP, Correy GJ, McCavitt-Malvido M, O'Leary PC, et al. A
571 single inactivating amino acid change in the SARS-CoV-2 NSP3 Mac1 domain attenuates
572 viral replication in vivo. PLoS Pathog. 2023;19(8):e1011614. Epub 20230831. doi:
573 10.1371/journal.ppat.1011614. PubMed PMID: 37651466; PubMed Central PMCID:
574 PMCPMC10499221.
575 27. Egloff MP, Malet H, Putics A, Heinonen M, Dutartre H, Frangeul A, et al. Structural and
576 functional basis for ADP-ribose and poly(ADP-ribose) binding by viral macro domains. J
577 Virol. 2006;80(17):8493-502. Epub 2006/08/17. doi: 10.1128/JVI.00713-06. PubMed PMID:
578 16912299; PubMed Central PMCID: PMCPMC1563857.
579 28. Grunewald ME, Chen Y, Kuny C, Maejima T, Lease R, Ferraris D, et al. The coronavirus
580 macrodomain is required to prevent PARP-mediated inhibition of virus replication and
581 enhancement of IFN expression. PLoS Pathog. 2019;15(5):e1007756. Epub 2019/05/17. doi:
582 10.1371/journal.ppat.1007756. PubMed PMID: 31095648; PubMed Central PMCID:
583 PMCPMC6521996.
584 29. Voth LS, O'Connor JJ, Kerr CM, Doerger E, Schwarting N, Sperstad P, et al. Unique
585 Mutations in the Murine Hepatitis Virus Macrodomain Differentially Attenuate Virus
586 Replication, Indicating Multiple Roles for the Macrodomain in Coronavirus Replication. J
587 Virol. 2021;95(15):e0076621. Epub 2021/05/21. doi: 10.1128/JVI.00766-21. PubMed PMID:
588 34011547; PubMed Central PMCID: PMCPMC8274620.
589 30. Luscher B, Ahel I, Altmeyer M, Ashworth A, Bai P, Chang P, et al. ADP-ribosyltransferases,
590 an update on function and nomenclature. FEBS J. 2021. Epub 20210729. doi:
591 10.1111/febs.16142. PubMed PMID: 34323016.
592 31. Eckei L, Krieg S, Butepage M, Lehmann A, Gross A, Lippok B, et al. The conserved
593 macrodomains of the non-structural proteins of Chikungunya virus and other pathogenic
594 positive strand RNA viruses function as mono-ADP-ribosylhydrolases. Sci Rep.
595 2017;7:41746. Epub 2017/02/06. doi: 10.1038/srep41746. PubMed PMID: 28150709;
596 PubMed Central PMCID: PMCPMC5288732.
597 32. Gupte R, Liu Z, Kraus WL. PARPs and ADP-ribosylation: recent advances linking molecular
598 functions to biological outcomes. Genes Dev. 2017;31(2):101-26. Epub 2017/02/17. doi:

599 10.1101/gad.291518.116. PubMed PMID: 28202539; PubMed Central PMCID:
600 PMCPMC5322727.
601 33. Atasheva S, Akhrymuk M, Frolova EI, Frolov I. New PARP gene with an anti-alphavirus
602 function. J Virol. 2012;86(15):8147-60. Epub 2012/05/25. doi: 10.1128/JVI.00733-12.
603 PubMed PMID: 22623789; PubMed Central PMCID: PMCPMC3421642.
604 34. Atasheva S, Frolova EI, Frolov I. Interferon-stimulated poly(ADP-Ribose) polymerases are
605 potent inhibitors of cellular translation and virus replication. J Virol. 2014;88(4):2116-30.
606 Epub 2013/12/18. doi: 10.1128/JVI.03443-13. PubMed PMID: 24335297; PubMed Central
607 PMCID: PMCPMC3911523.
608 35. Daugherty MD, Young JM, Kerns JA, Malik HS. Rapid evolution of PARP genes suggests a
609 broad role for ADP-ribosylation in host-virus conflicts. PLoS Genet. 2014;10(5):e1004403.
610 Epub 2014/05/31. doi: 10.1371/journal.pgen.1004403. PubMed PMID: 24875882; PubMed
611 Central PMCID: PMCPMC4038475.
612 36. Fehr AR, Singh SA, Kerr CM, Mukai S, Higashi H, Aikawa M. The impact of PARPs and
613 ADP-ribosylation on inflammation and host-pathogen interactions. Genes Dev. 2020;34(5-
614 6):341-59. Epub 2020/02/08. doi: 10.1101/gad.334425.119. PubMed PMID: 32029454;
615 PubMed Central PMCID: PMCPMC7050484.
616 37. Gao G, Guo X, Goff SP. Inhibition of retroviral RNA production by ZAP, a CCCH-type zinc
617 finger protein. Science. 2002;297(5587):1703-6. Epub 2002/09/07. doi:
618 10.1126/science.1074276. PubMed PMID: 12215647.
619 38. Li L, Shi Y, Li S, Liu J, Zu S, Xu X, et al. ADP-ribosyltransferase PARP11 suppresses Zika
620 virus in synergy with PARP12. Cell Biosci. 2021;11(1):116. Epub 20210629. doi:
621 10.1186/s13578-021-00628-y. PubMed PMID: 34187568; PubMed Central PMCID:
622 PMCPMC8240438.
623 39. Li L, Zhao H, Liu P, Li C, Quanquin N, Ji X, et al. PARP12 suppresses Zika virus infection
624 through PARP-dependent degradation of NS1 and NS3 viral proteins. Sci Signal.
625 2018;11(535). Epub 2018/06/21. doi: 10.1126/scisignal.aas9332. PubMed PMID: 29921658;
626 PubMed Central PMCID: PMCPMC6434931.
627 40. Liu CH, Zhou L, Chen G, Krug RM. Battle between influenza A virus and a newly identified
628 antiviral activity of the PARP-containing ZAPL protein. Proc Natl Acad Sci U S A.
629 2015;112(45):14048-53. Epub 2015/10/28. doi: 10.1073/pnas.1509745112. PubMed PMID:
630 26504237; PubMed Central PMCID: PMCPMC4653199.
631 41. Kerr CM, Parthasarathy S, Schwarting N, O'Connor JJ, Pfannenstiel JJ, Giri E, et al. PARP12
632 is required to repress the replication of a Mac1 mutant coronavirus in a cell- and tissue-
633 specific manner. J Virol. 2023;97(9):e0088523. Epub 20230911. doi: 10.1128/jvi.00885-23.
634 PubMed PMID: 37695054; PubMed Central PMCID: PMCPMC10537751.
635 42. Ruby J, Ramshaw I. The antiviral activity of immune CD8+ T cells is dependent on
636 interferon-gamma. Lymphokine Cytokine Res. 1991;10(5):353-8. PubMed PMID: 1768738.
637 43. Lee BNR, Chang HK, Son YS, Lee D, Kwon SM, Kim PH, et al. IFN-gamma enhances the
638 wound healing effect of late EPCs (LEPCs) via BST2-mediated adhesion to endothelial cells.
639 FEBS Lett. 2018;592(10):1705-15. Epub 20180516. doi: 10.1002/1873-3468.13078. PubMed
640 PMID: 29710419.
641 44. Thapa M, Kuziel WA, Carr DJ. Susceptibility of CCR5-deficient mice to genital herpes
642 simplex virus type 2 is linked to NK cell mobilization. J Virol. 2007;81(8):3704-13. Epub
643 20070131. doi: 10.1128/JVI.02626-06. PubMed PMID: 17267483; PubMed Central PMCID:
644 PMCPMC1866094.

645 45. Bot A, Bot S, Bona CA. Protective role of gamma interferon during the recall response to
646 influenza virus. J Virol. 1998;72(8):6637-45. doi: 10.1128/JVI.72.8.6637-6645.1998.
647 PubMed PMID: 9658110; PubMed Central PMCID: PMCPMC109853.
648 46. Hilligan KL, Namasivayam S, Clancy CS, Baker PJ, Old SI, Peluf V, et al. Bacterial-induced
649 or passively administered interferon gamma conditions the lung for early control of SARS-
650 CoV-2. Nat Commun. 2023;14(1):8229. Epub 20231212. doi: 10.1038/s41467-023-43447-0.
651 PubMed PMID: 38086794; PubMed Central PMCID: PMCPMC10716133.
652 47. Parra B, Hinton DR, Lin MT, Cua DJ, Stohlman SA. Kinetics of cytokine mRNA expression
653 in the central nervous system following lethal and nonlethal coronavirus-induced acute
654 encephalomyelitis. Virology. 1997;233(2):260-70. doi: 10.1006/viro.1997.8613. PubMed
655 PMID: 9217050; PubMed Central PMCID: PMCPMC7131685.
656 48. Parra B, Hinton DR, Marten NW, Bergmann CC, Lin MT, Yang CS, et al. IFN-gamma is
657 required for viral clearance from central nervous system oligodendroglia. J Immunol.
658 1999;162(3):1641-7. PubMed PMID: 9973424.
659 49. Liu SY, Sanchez DJ, Aliyari R, Lu S, Cheng G. Systematic identification of type I and type
660 II interferon-induced antiviral factors. Proc Natl Acad Sci U S A. 2012;109(11):4239-44.
661 Epub 2012/03/01. doi: 10.1073/pnas.1114981109. PubMed PMID: 22371602; PubMed
662 Central PMCID: PMCPMC3306696.
663 50. Parthasarathy S, Saenjamsai P, Hao H, Ferkul A, Pfannenstiel JJ, Suder EL, et al. PARP14 is
664 pro- and anti-viral host factor that promotes IFN production and affects the replication of
665 multiple viruses. bioRxiv. 2024. Epub 20240426. doi: 10.1101/2024.04.26.591186. PubMed
666 PMID: 38712082; PubMed Central PMCID: PMCPMC11071520.
667 51. Janach GMS, Reetz O, Dohne N, Stadler K, Grosser S, Byvaltcev E, et al. Interferon-gamma
668 acutely augments inhibition of neocortical layer 5 pyramidal neurons. J Neuroinflammation.
669 2020;17(1):69. Epub 20200222. doi: 10.1186/s12974-020-1722-y. PubMed PMID:
670 32087716; PubMed Central PMCID: PMCPMC7035745.
671 52. Sun L, Tian Z, Wang J. A direct cross-talk between interferon-gamma and sonic hedgehog
672 signaling that leads to the proliferation of neuronal precursor cells. Brain Behav Immun.
673 2010;24(2):220-8. Epub 20091002. doi: 10.1016/j.bbi.2009.09.016. PubMed PMID:
674 19800966; PubMed Central PMCID: PMCPMC2821661.
675 53. Makela J, Koivuniemi R, Korhonen L, Lindholm D. Interferon-gamma produced by
676 microglia and the neuropeptide PACAP have opposite effects on the viability of neural
677 progenitor cells. PLoS One. 2010;5(6):e11091. Epub 20100614. doi:
678 10.1371/journal.pone.0011091. PubMed PMID: 20559421; PubMed Central PMCID:
679 PMCPMC2885411.
680 54. Wang X, Suzuki Y. Microglia produce IFN-gamma independently from T cells during acute
681 toxoplasmosis in the brain. J Interferon Cytokine Res. 2007;27(7):599-605. doi:
682 10.1089/jir.2006.0157. PubMed PMID: 17651021.
683 55. Sa Q, Ochiai E, Tiwari A, Perkins S, Mullins J, Gehman M, et al. Cutting Edge: IFN-gamma
684 Produced by Brain-Resident Cells Is Crucial To Control Cerebral Infection with Toxoplasma
685 gondii. J Immunol. 2015;195(3):796-800. Epub 20150619. doi: 10.4049/jimmunol.1500814.
686 PubMed PMID: 26091720; PubMed Central PMCID: PMCPMC4520543.
687 56. Suzuki Y, Claflin J, Wang X, Lengi A, Kikuchi T. Microglia and macrophages as innate
688 producers of interferon-gamma in the brain following infection with Toxoplasma gondii. Int
689 J Parasitol. 2005;35(1):83-90. Epub 20041208. doi: 10.1016/j.ijpara.2004.10.020. PubMed
690 PMID: 15619519.

691 57. Dobin A, Davis CA, Schlesinger F, Drenkow J, Zaleski C, Jha S, et al. STAR: ultrafast
692 universal RNA-seq aligner. Bioinformatics. 2013;29(1):15-21. Epub 20121025. doi:
693 10.1093/bioinformatics/bts635. PubMed PMID: 23104886; PubMed Central PMCID:
694 PMCPMC3530905.
695 58. Li B, Dewey CN. RSEM: accurate transcript quantification from RNA-Seq data with or
696 without a reference genome. BMC Bioinformatics. 2011;12:323. Epub 20110804. doi:
697 10.1186/1471-2105-12-323. PubMed PMID: 21816040; PubMed Central PMCID:
698 PMCPMC3163565.
699 59. Love MI, Huber W, Anders S. Moderated estimation of fold change and dispersion for RNA-
700 seq data with DESeq2. Genome Biol. 2014;15(12):550. doi: 10.1186/s13059-014-0550-8.
701 PubMed PMID: 25516281; PubMed Central PMCID: PMCPMC4302049.
702 60. Zhu A, Ibrahim JG, Love MI. Heavy-tailed prior distributions for sequence count data:
703 removing the noise and preserving large differences. Bioinformatics. 2019;35(12):2084-92.
704 doi: 10.1093/bioinformatics/bty895. PubMed PMID: 30395178; PubMed Central PMCID:
705 PMCPMC6581436.
706
707

708 **FIGURE LEGENDS**

709 **Fig 1. JHMV N1347A has decreased replication in the olfactory bulbs of mice.** (A-C) C57BL/6
710 mice were infected with infected i.n. with 10^4 PFU of JHMV WT or N1347A. Brains were
711 harvested at 5 dpi and viral load was determined via plaque assay (A), genomic RNA levels
712 (gRNA) were determined by RT-qPCR (B) and olfactory bulb sections were stained for MHV
713 nucleocapsid protein (yellow), NISSL (Neurotrace™, red), and DAPI (blue) by IHC (C). The data
714 in A is the combined results of 3 independent experiments. n=13 mice per group. The data in B is
715 the combined result of 2 independent experiments. n=4 mice (WT) and n=6 mice (N1347A). The
716 images in C are from 1 experiment representative of 2 independent experiments. Scale bar is 100
717 μm. n=2-4 mice per group. Statistics were determined using a Mann-Whitney t-test.

718 **Fig 2. IFNγ and several PARP genes are upregulated in infected olfactory bulbs of JHMV**
719 **infected mice.** (A) C57BL/6 mice were either mock infected or infected i.n. with 1×10^4 PFU
720 N1347A virus. Olfactory bulbs were harvested at 5 dpi in Trizol, and total RNA was isolated. The
721 total RNA from the samples were analyzed by RNAseq to determine the full transcriptome in the
722 olfactory bulb following infection and is represented by a volcano plot indicating *d*ifferentially
723 *e*xpressed *g*enes (DEGs) between mock and N1347A infected mice. Vertical dashed lines highlight
724 absolute log2 fold-change (LFC) values > 2. Genes that are significant and have LFC values > 2
725 are shown in red, those that are significant but with LFC values < 2 are in blue, genes that are not
726 significant but have LFC values > 2 are in yellow, and genes that are not significant and with LFC
727 values < 2 are in grey. n=2 mice (mock); n=3 mice (N1347A). (B) Normalized counts of individual
728 IFN genes between mock and N1347A infected mice from the RNAseq data show in 2A were
729 calculated and represented in form of a bar graph. (C) C57BL/6 mice were either mock infected
730 or infected i.n. with 1×10^4 PFU WT or N1347A virus. Olfactory bulbs were harvested at 5 dpi in

731 Trizol, and total RNA was isolated. The levels of IFNβ and IFNγ mRNA transcripts were analyzed
732 by qRT-PCR normalized to HPRT. n=3 mice (mock); n=5 mice (WT); n=8 mice (N1347A).
733 Statistics were determined using a 2-way ANOVA. (D) C57BL/6 mice were either mock infected
734 or infected i.n. with 1×10^4 PFU N1347A virus. Olfactory bulbs were harvested at 5 dpi in Trizol,
735 and total RNA was isolated. The levels of PARP mRNA transcripts were analyzed by qRT-PCR
736 normalized to HPRT. n=6 mice (mock); n=6 mice (N1347A). Statistics were determined using a
737 Mann-Whitney t-test.

738 **Fig 3. JHMV replicates poorly in the brains of IFN-γ and IFNγR null mice.** (A-B) C57BL/6
739 WT, IFN-$\gamma^{-/-}$, and IFN-γR$^{-/-}$ mice were infected i.n. with 1×10^4 PFU WT or N1347A virus.
740 Olfactory bulbs (OB) (A) or whole brains (B) were harvested at 5 dpi and viral loads were
741 measured by plaque assay. Data from WT mice in (A) is the same data in Fig. 1A. It is placed here
742 as a comparison to the other genotypes. (A) n=13 (WT/WT), n=13 (WT/N1347A), n=8 (IFN-$\gamma^{-/-}$
743 /WT), n=9 (IFN-$\gamma^{-/-}$/N1347A), n=10 (IFN-γR$^{-/-}$/WT), n=11 (IFN-γR$^{-/-}$/N1347A). (B) n=6
744 (WT/WT), n=6 (WT/N1347A), n=8 (IFN-$\gamma^{-/-}$/WT), n=9 (IFN-$\gamma^{-/-}$/N1347A), n=10 (IFN-γR$^{-/-}$/WT),
745 n=11 (IFNγR$^{-/-}$/N1347A). Statistics were determined by a one-way ANOVA. (C-D) Indicated
746 mouse strains were infected i.n. with 1×10^4 PFU WT virus. Olfactory bulbs (C) or whole brains
747 (D) were harvested a 5 dpi and viral genomic and sub-genomic RNA was measured by RT-qPCR.
748 n=3 (WT/WT), n=5 (IFN-$\gamma^{-/-}$/WT), n=10 (IFN-γR$^{-/-}$/WT). Statistics were determined by a one-way
749 ANOVA. (E) C57BL/6 WT, and IFN-$\gamma^{-/-}$ cells were infected i.n. with 1×10^4 PFU WT or N1347A
750 virus. At 5 dpi olfactory bulbs were fixed and sections were stained for MHV nucleocapsid (N)
751 protein (yellow) by IHC. Each image represents a different mouse. n=2 mice for each group. Each
752 image represents a different mouse and WT images include images from the same mice as in Fig.
753 1. Co-staining of images with DAPI (nuclei) and Nissl (Neurotrace^{TM}) as controls can be seen in

754 Fig. S1. (F) Quantification of all images taken for each group. Each dot represents a different
755 image. Statistics were determined using a 2-way ANOVA.

756 **Fig 4. JHMV survival and weight loss is not altered IFN-γ null mice.** (A-B) C57BL/6 WT,
757 IFN-$\gamma^{-/-}$, and IFN-γR$^{-/-}$ mice were infected i.n. with 1×10^4 (A-B), 3×10^3 (C-D), or 1×10^3 (E-F) PFU
758 WT virus. Mice were monitored daily for survival (A,C,E) and weight loss (B,D,F). (A-B) n=6
759 (WT), n=3 (IFN-$\gamma^{-/-}$), n=7 (IFN-γR$^{-/-}$). (C-D) n=4 (WT), n=4 (IFN-$\gamma^{-/-}$), n=5 (IFN-γR$^{-/-}$). (E-F) n=5
760 (WT), n=4 (IFN-$\gamma^{-/-}$), n=5 (IFN-γR$^{-/-}$). Statistics were determined using a Kaplan-Meier survival
761 analysis (A,C,E) or an ordinary one-way ANOVA (B,D,F).

762 **Fig 5. JHMV replication is unaffected by the lack of IFN-γ and is repressed by the addition**
763 **of exogenous IFN-γ in bone-marrow derived macrophages .** (A) C57BL/6 WT, IFN-$\gamma^{-/-}$, and
764 IFN-γR$^{-/-}$ bone-marrow derived macrophages (BMDMs) were harvested from mice and
765 differentiated into M2 macrophages as described in Methods. BMDMs were infected with WT and
766 N1347A virus at an MOI of 0.1 and cells and supernatants were collected at indicated time points
767 and infectious virus was measured by plaque assay. (B) BMDMs were pretreated with IFN-γ for
768 20 hr and then infected with JHMV at an MOI of 0.1 and cells and supernatants were collected at
769 indicated time points and infectious virus was measured by plaque assay. (A-B) are from one
770 experiment representative of two independent experiments. Statistics in A-B were determined by
771 an ordinary one-way ANOVA.

772 **Fig 6. WT and IFN-γR-/- have similar amounts of cytokines and frequencies of immune cells**
773 **in the brain following infection.** (A) C57BL/6 WT, IFN-$\gamma^{-/-}$, or IFN-γR$^{-/-}$ mice were infected i.n.
774 with 1×10^4 PFU WT virus. Olfactory bulbs (left panel) and whole brains (right panel) were
775 harvested at 5 dpi and total RNA was collected and cytokine mRNA was measured by RT-qPCR,
776 normalized to HPRT. n=3 mice (WT); n=5 mice (IFN-$\gamma^{-/-}$); n=5 mice (IFN-γR$^{-/-}$) . Statistics were

777 determined using an ordinary one-way ANOVA. (B) C57BL/6 WT or IFNγR-/- mice were either
778 mock infected or infected i.n. with 1×10^4 PFU WT virus. Whole brains were harvested at 5 dpi
779 and cells were stained for immune cell markers and analyzed by flow cytometry. n=17 mice
780 (mock); n=13 mice (WT); n=16 mice (IFN-γR-/-). Statistics were determined using an ordinary
781 one-way ANOVA.

782 **Fig 7. IFN-γ is produced by microglia, CD4+ T cells, and macrophages in the brains of JHMV**
783 **infected mice.** C57BL/6 WT or IFN-γR-/- mice were either mock infected or infected i.n. with
784 1×10^4 PFU WT virus. Whole brains were harvested at 5 dpi and IFNγ staining from each cell
785 population was analyzed by flow cytometry. (A) The frequency of IFN-γ+ cells and (B) expression
786 of IFN-γ (gMFI) for each cell type shown. Cell types analyzed were microglia (plum, circle),
787 CD4+ T cells (magenta, square), CD8 T cells (bright pink, triangle), NK cells (carnation,
788 diamond), DCs (pink, hexagon), and macrophages (purple, upside down triangle). Each point
789 represents a mouse. The data in (A) is a pooled data from 3 independent studies while the data in
790 (B) is from a representative experiment. Statistics were determined using a two-way ANOVA.

791 **SUPPLEMENTAL FIGURE LEGENDS**

792 **Fig S1. JHMV replicates poorly in the brains of IFN-γ null mice.** C57BL/6 WT and IFN-$\gamma^{-/-}$
793 mice were infected i.n. with 1×10^4 PFU WT or N1347A virus. At 5 dpi olfactory bulbs were fixed
794 and sections were stained for MHV nucleocapsid (N) protein (yellow), DAPI (nuclei - blue) and
795 Neurotrace™ (red) by IHC. n=2 mice for each group. Shown are two representative images for
796 each mouse.

797 **Fig S2. The loss of IFNγ in bone-marrow derived macrophages does not impact JHMV**
798 **replication.** C57BL/6 WT, IFN$\gamma^{-/-}$, and IFNγR$^{-/-}$ bone-marrow derived macrophages (BMDMs)
799 were harvested from mice and differentiated into M2 macrophages as previously described.

800 BMDMs were infected with WT and N1347A virus at an MOI of 0.1 and cells were collected at
801 20 hpi. RNA was harvested and JHMV genomic RNA was measured by qPCR. Data are from one
802 experiment representative of two independent experiments. Statistics were determined by an
803 ordinary one-way ANOVA.

804 **Fig S3. Gating strategy for immune cells.**

805 **Fig S4. Representative IFN-γ histograms in different cell populations.**

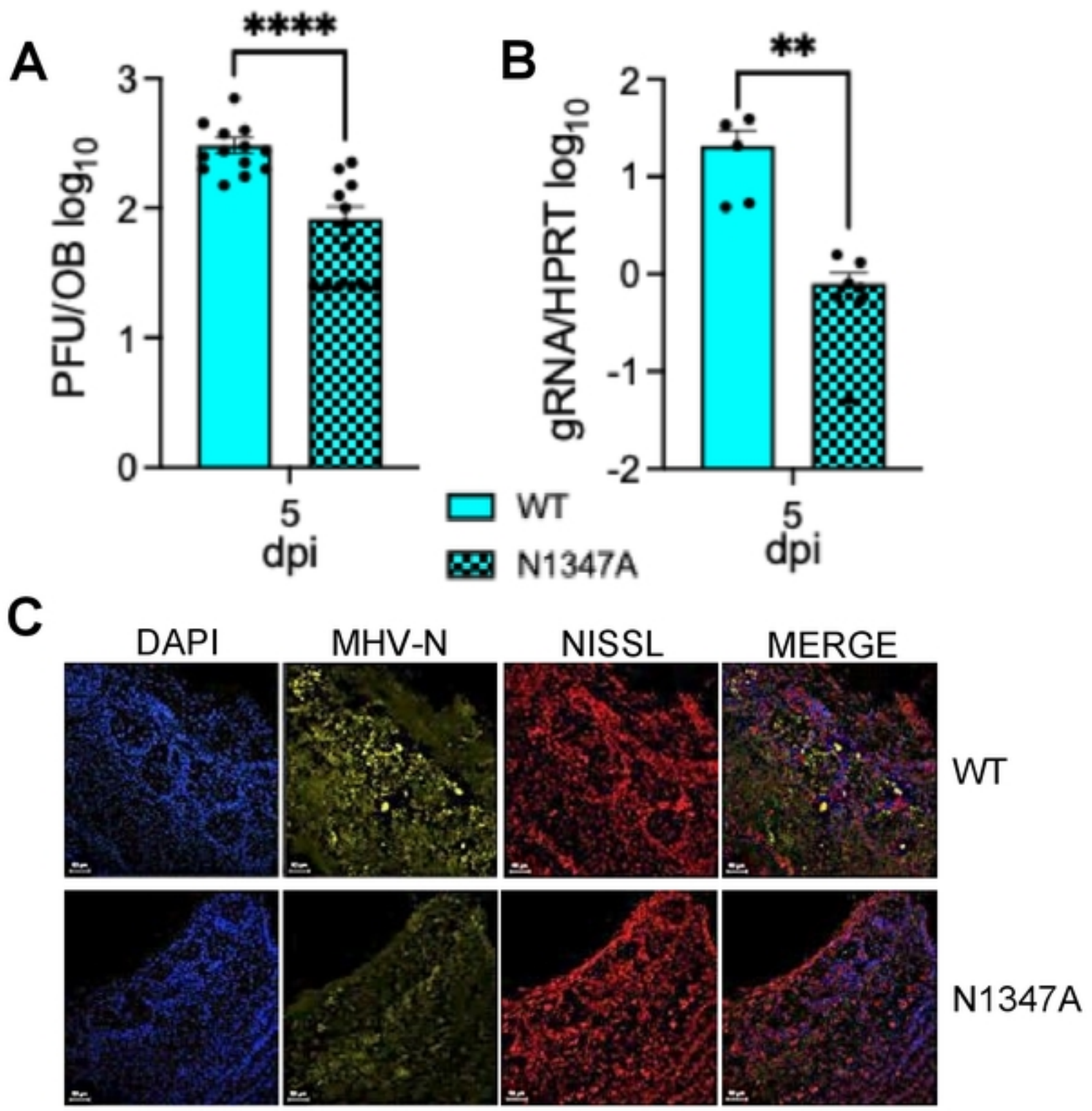

Fig 1. JHMV N1347A has decreased replication in the olfactory bulbs of mice. (A-C) C57BL/6 mice were infected with infected i.n. with 10^4 PFU of JHMV WT or N1347A. Brains were harvested at 5 dpi and viral load was determined via plaque assay (A), genomic RNA levels (gRNA) were determined by RT-qPCR (B) and olfactory bulb sections were stained for MHV nucleocapsid protein (yellow), NISSL (Neurotrace™, red), and DAPI (blue) by IHC (C). The data in A is the combined results of 3 independent experiments. n=13 mice per group. The data in B is the combined result of 2 independent experiments. n=4 mice (WT) and n=6 mice (N1347A). The images in C are from 1 experiment representative of 2 independent experiments. Scale bar is 100 μm. n=2-4 mice per group. Statistics were determined using a Mann-Whitney t-test.

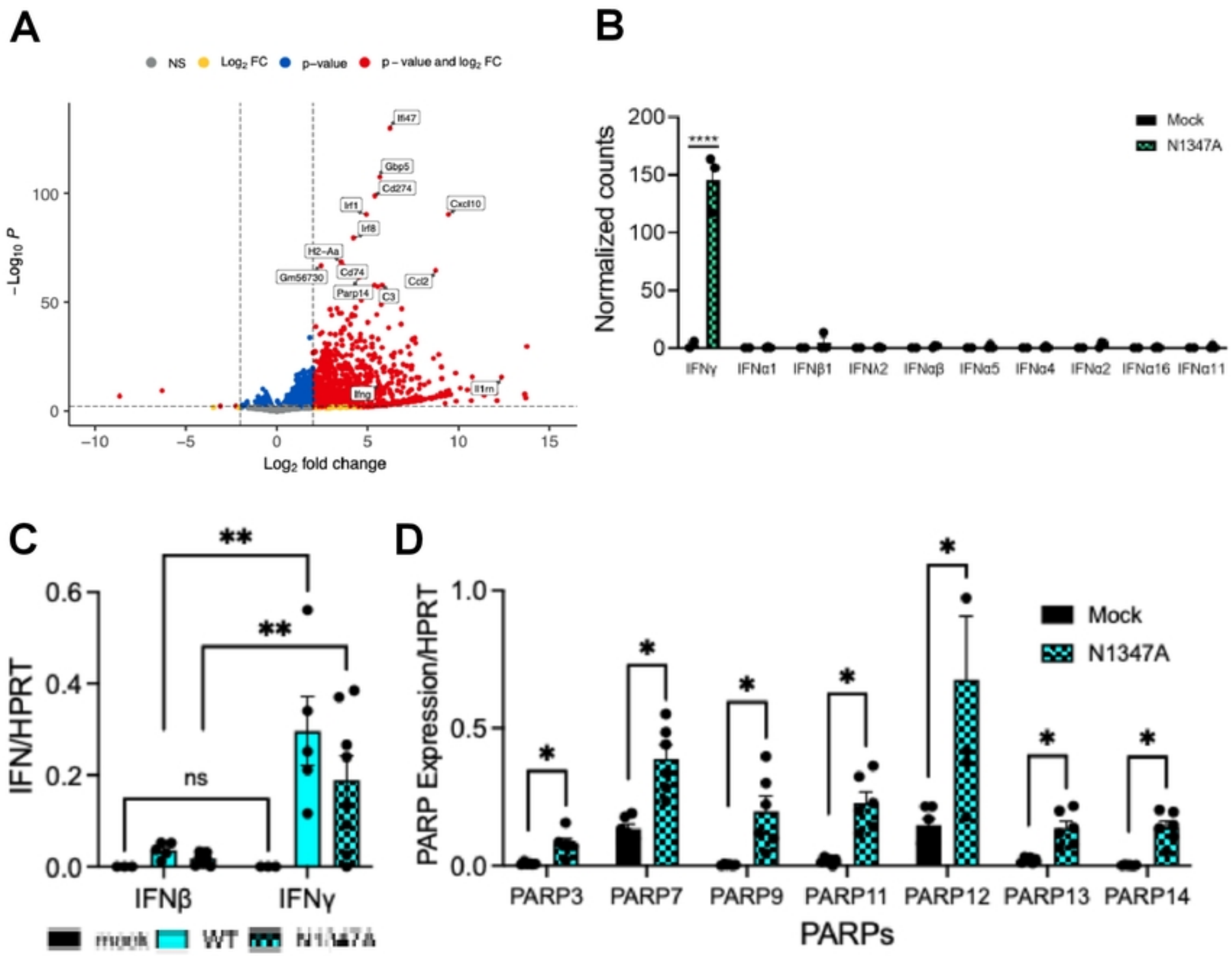

Fig 2. IFNγ and several PARP genes are upregulated in infected olfactory bulbs of JHMV infected mice. (A) C57BL/6 mice were either mock infected or infected i.n. with 1×10^4 PFU N1347A virus. Olfactory bulbs were harvested at 5 dpi in Trizol, and total RNA was isolated. The total RNA from the samples were analyzed by RNAseq to determine the full transcriptome in the olfactory bulb following infection and is represented by a volcano plot indicating differentially expressed genes (DEGs) between mock and N1347A infected mice. Vertical dashed lines highlight absolute log2 fold-change (LFC) values > 2. Genes that are significant and have LFC values > 2 are shown in red, those that are significant but with LFC values < 2 are in blue, genes that are not significant but have LFC values > 2 are in yellow, and genes that are not significant and with LFC values < 2 are in grey. n=2 mice (mock); n=3 mice (N1347A). (B) Normalized counts of individual IFN genes between mock and N1347A infected mice from the RNAseq data show in 2A were calculated and represented in form of a bar graph. (C) C57BL/6 mice were either mock infected or infected i.n. with 1×10^4 PFU WT or N1347A virus. Olfactory bulbs were harvested at 5 dpi in Trizol, and total RNA was isolated. The levels of IFNβ and IFNγ mRNA transcripts were analyzed by qRT-PCR normalized to HPRT. n=3 mice (mock); n=5 mice (WT); n=8 mice (N1347A). Statistics were determined using a 2-way ANOVA. (D) C57BL/6 mice were either mock infected or infected i.n. with 1×10^4 PFU N1347A virus. Olfactory bulbs were harvested at 5 dpi in Trizol, and total RNA was isolated. The levels of PARP mRNA transcripts were analyzed by qRT-PCR normalized to HPRT. n=6 mice (mock); n=6 mice (N1347A). Statistics were determined using a Mann-Whitney t-test.

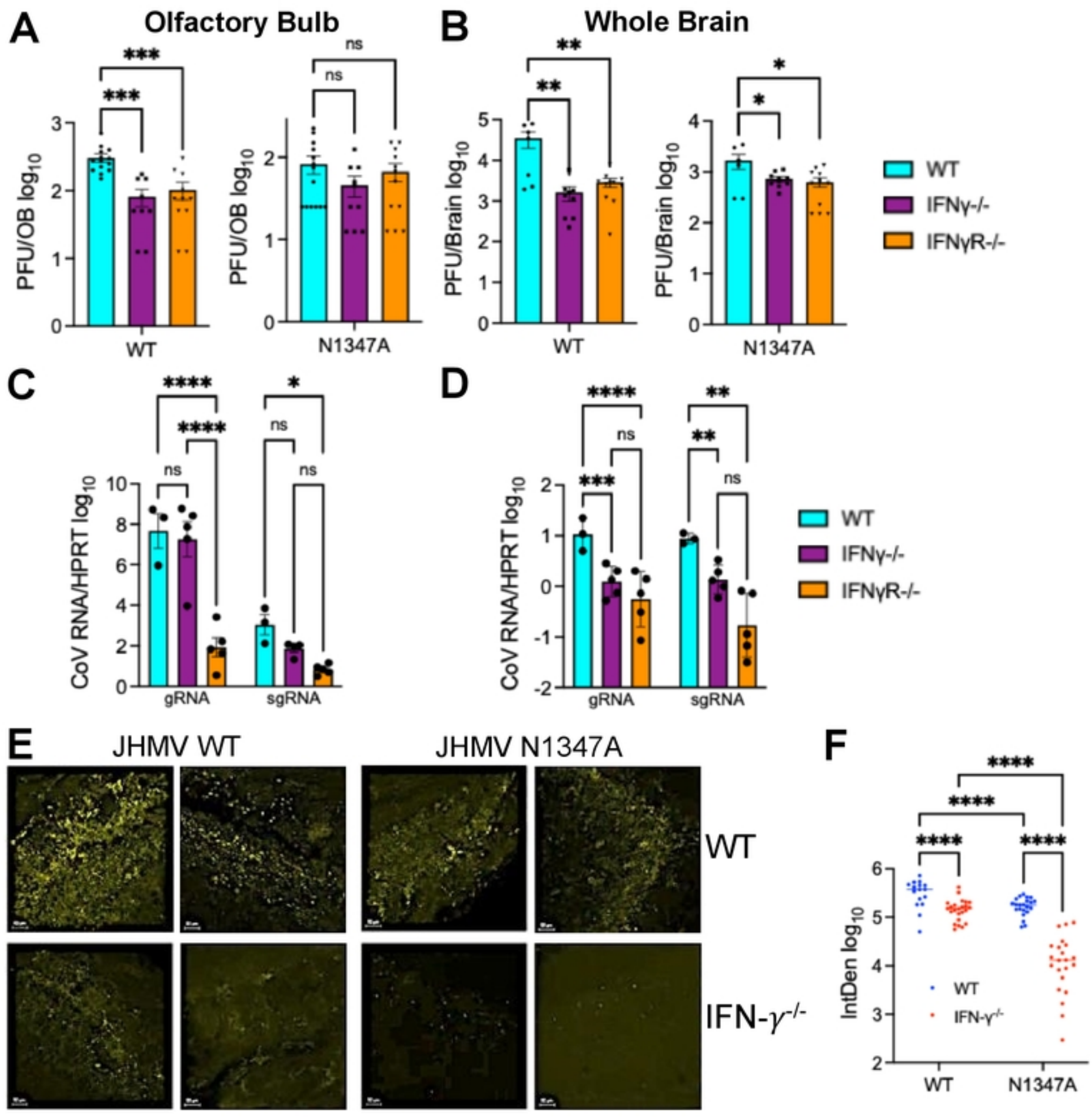

Fig 3. JHMV replicates poorly in the brains of IFN-γ and IFNγR null mice. (A-B) C57BL/6 WT, IFN-$\gamma^{-/-}$, and IFN-$\gamma R^{-/-}$ mice were infected i.n. with 1×10^4 PFU WT or N1347A virus. Olfactory bulbs (OB) (A) or whole brains (B) were harvested at 5 dpi and viral loads were measured by plaque assay. Data from WT mice in (A) is the same data in Fig. 1A. It is placed here as a comparison to the other genotypes. (A) n=13 (WT/WT), n=13 (WT/N1347A), n=8 (IFN-$\gamma^{-/-}$/WT), n=9 (IFN-$\gamma^{-/-}$/N1347A), n=10 (IFN-$\gamma R^{-/-}$/WT), n=11 (IFN-$\gamma R^{-/-}$/N1347A). (B) n=6 (WT/WT), n=6 (WT/N1347A), n=8 (IFN-$\gamma^{-/-}$/WT), n=9 (IFN-$\gamma^{-/-}$/N1347A), n=10 (IFN-$\gamma R^{-/-}$/WT), n=11 (IFN$\gamma R^{-/-}$/N1347A). Statistics were determined by a one-way ANOVA. (C-D) Indicated mouse strains were infected i.n. with 1×10^4 PFU WT virus. Olfactory bulbs (C) or whole brains (D) were harvested a 5 dpi and viral genomic and sub-genomic RNA was measured by RT-qPCR. n=3 (WT/WT), n=5 (IFN-$\gamma^{-/-}$/WT), n=10 (IFN-$\gamma R^{-/-}$/WT). Statistics were determined by a one-way ANOVA. (E) C57BL/6 WT, and IFN-$\gamma^{-/-}$ cells were infected i.n. with 1×10^4 PFU WT or N1347A virus. At 5 dpi olfactory bulbs were fixed and sections were stained for MHV nucleocapsid (N) protein (yellow) by IHC. Each image represents a different mouse. n=2 mice for each group. Each image represents a different mouse and WT images include images from the same mice as in Fig. 1. Co-staining of images with DAPI (nuclei) and Nissl (Neurotrace™) as controls can be seen in Fig. S1. (F) Quantification of all images taken for each group. Each dot represents a different image. Statistics were determined using a 2-way ANOVA.

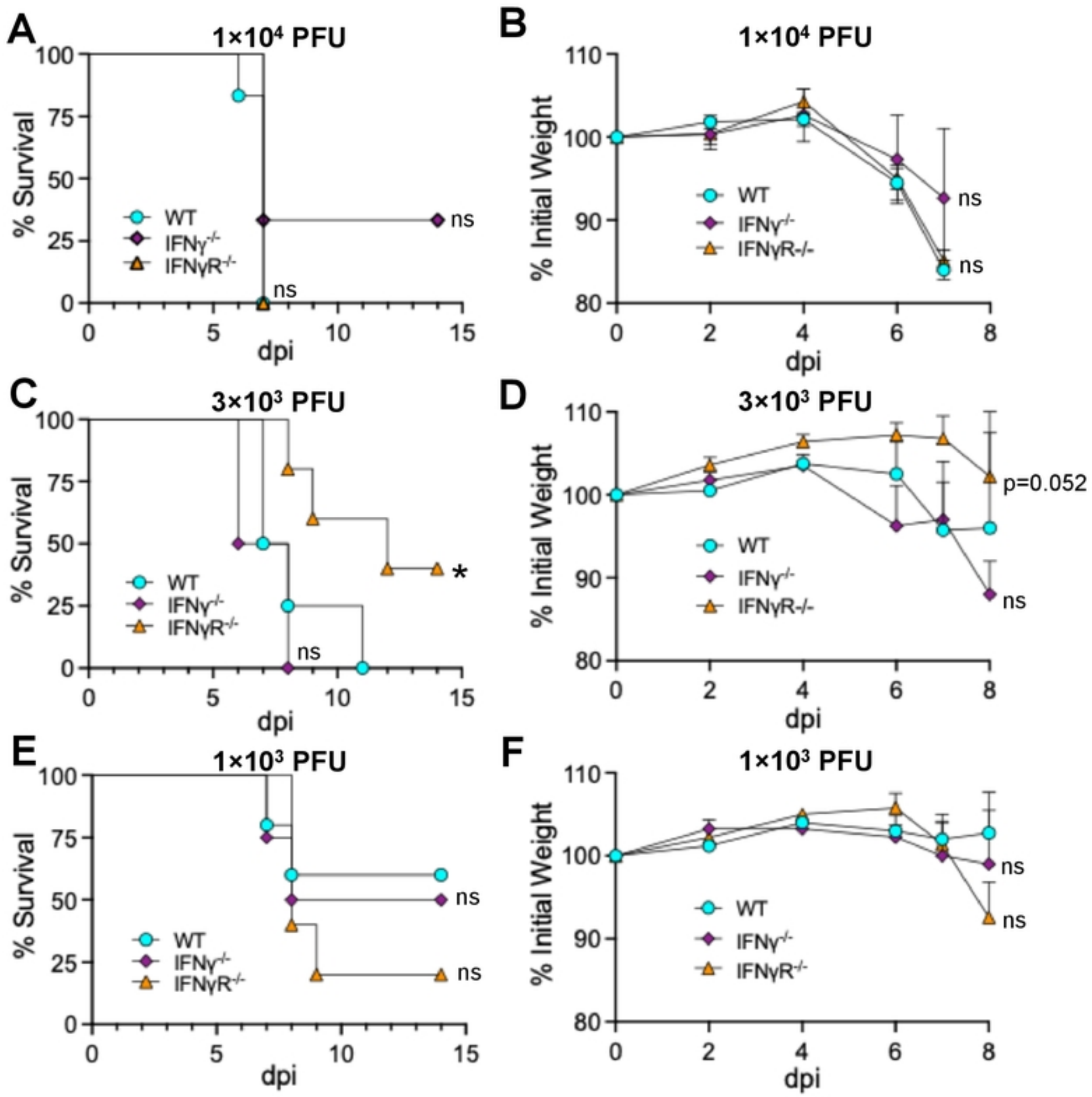

Fig 4. JHMV survival and weight loss is not altered IFN-γ null mice. (A-B) C57BL/6 WT, IFN-$\gamma^{-/-}$, and IFN-$\gamma R^{-/-}$ mice were infected i.n. with 1×10^4 (A-B), 3×10^3 (C-D), or 1×10^3 (E-F) PFU WT virus. Mice were monitored daily for survival (A,C,E) and weight loss (B,D,F). (A-B) n=6 (WT), n=3 (IFN-$\gamma^{-/-}$), n=7 (IFN-$\gamma R^{-/-}$). (C-D) n=4 (WT), n=4 (IFN-$\gamma^{-/-}$), n=5 (IFN-$\gamma R^{-/-}$). (E-F) n=5 (WT), n=4 (IFN-$\gamma^{-/-}$), n=5 (IFN-$\gamma R^{-/-}$). Statistics were determined using a Kaplan-Meier survival analysis (A,C,E) or an ordinary one-way ANOVA (B,D,F).

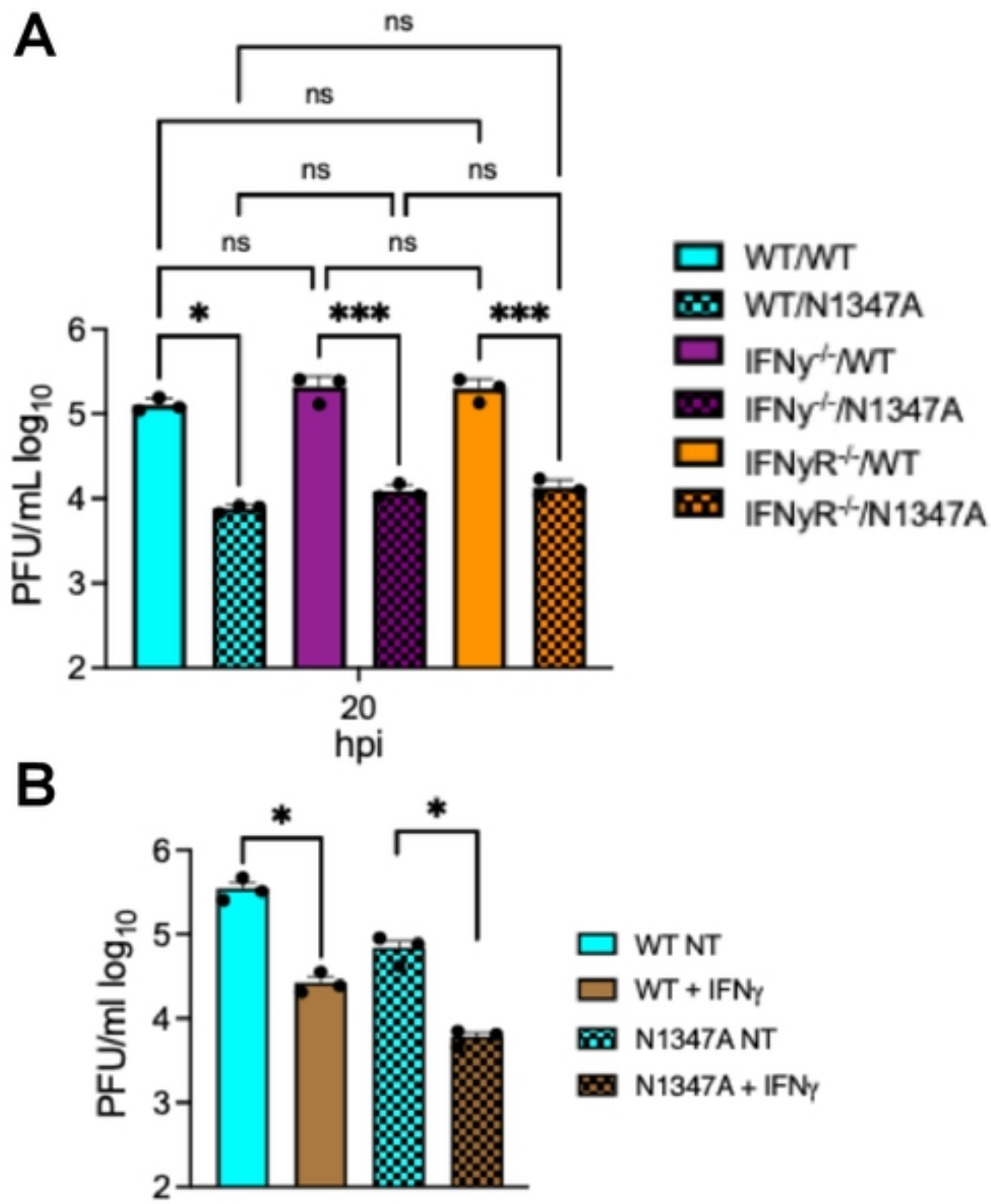

Fig 5. JHMV replication is unaffected by the lack of IFN-γ and is repressed by the addition of exogenous IFN-γ in bone-marrow derived macrophages . (A) C57BL/6 WT, IFN-$\gamma^{-/-}$, and IFN-γR$^{-/-}$ bone-marrow derived macrophages (BMDMs) were harvested from mice and differentiated into M2 macrophages as described in Methods. BMDMs were infected with WT and N1347A virus at an MOI of 0.1 and cells and supernatants were collected at indicated time points and infectious virus was measured by plaque assay. (B) BMDMs were pretreated with IFN-γ for 20 hr and then infected with JHMV at an MOI of 0.1 and cells and supernatants were collected at indicated time points and infectious virus was measured by plaque assay. (A-B) are from one experiment representative of two independent experiments. Statistics in A-B were determined by an ordinary one-way ANOVA.

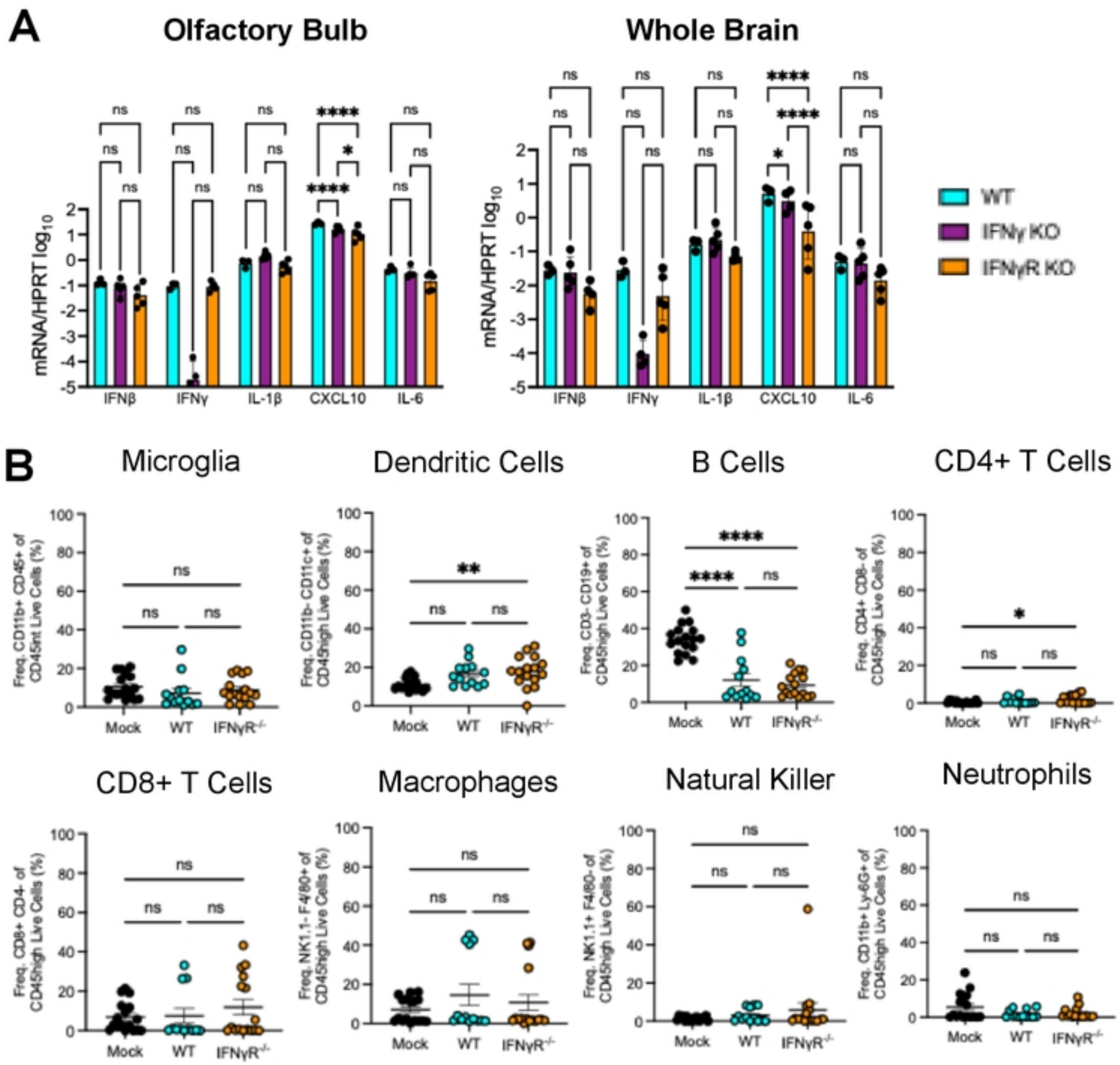

Fig 6. WT and IFN-γR-/- have similar amounts of cytokines and frequencies of immune cells in the brain following infection. (A) C57BL/6 WT, IFN-$\gamma^{-/-}$, or IFN-$\gamma R^{-/-}$ mice were infected i.n. with 1×10^4 PFU WT virus. Olfactory bulbs (left panel) and whole brains (right panel) were harvested at 5 dpi and total RNA was collected and cytokine mRNA was measured by RT-qPCR, normalized to HPRT. n=3 mice (WT); n=5 mice (IFN-$\gamma^{-/-}$); n=5 mice (IFN-$\gamma R^{-/-}$) . Statistics were determined using an ordinary one-way ANOVA. (B) C57BL/6 WT or IFNγR-/- mice were either mock infected or infected i.n. with 1×10^4 PFU WT virus. Whole brains were harvested at 5 dpi and cells were stained for immune cell markers and analyzed by flow cytometry. n=17 mice (mock); n=13 mice (WT); n=16 mice (IFN-γR-/-). Statistics were determined using an ordinary one-way ANOVA.

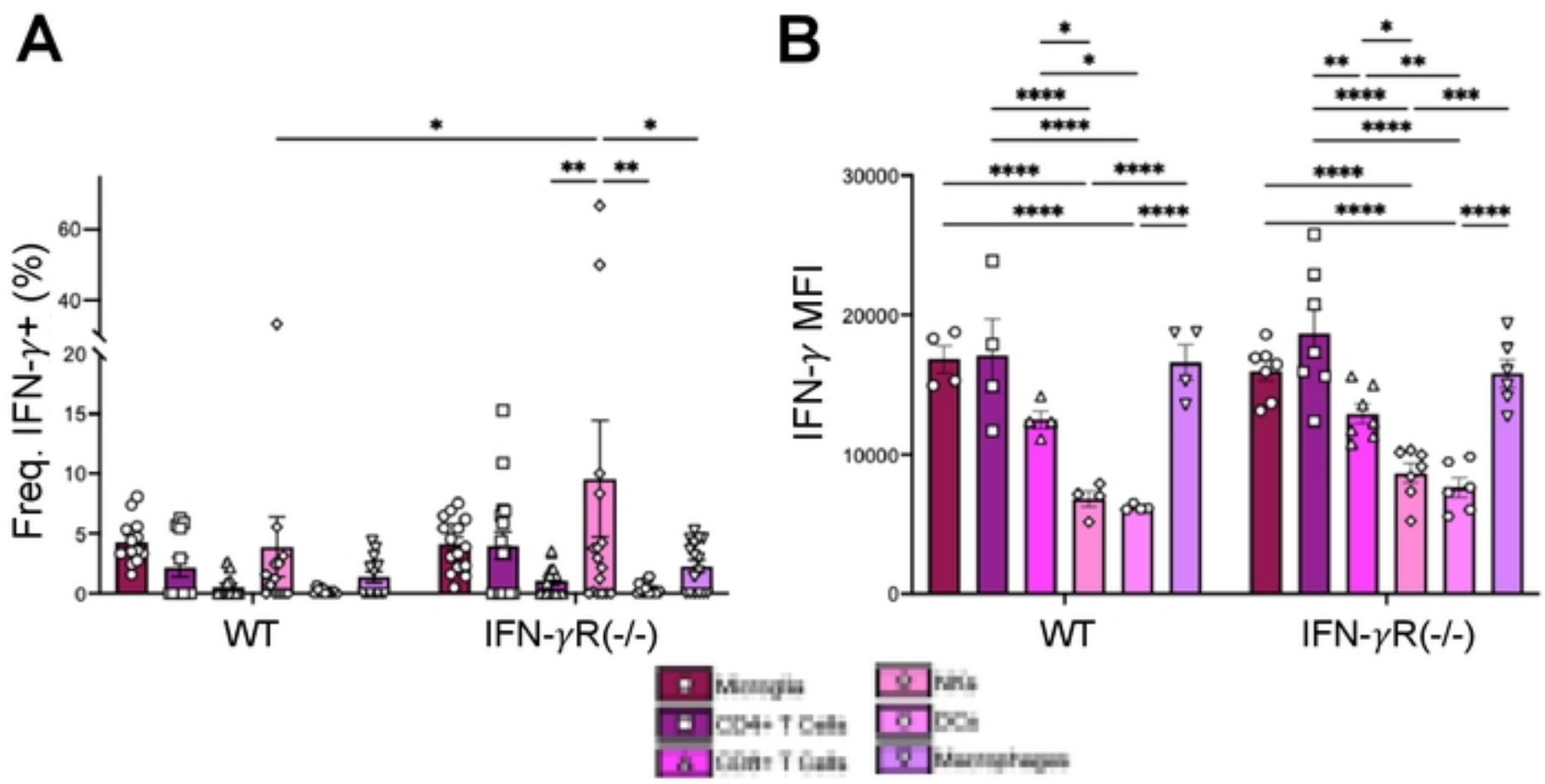

Fig 7. IFN-γ is produced by microglia, CD4+ T cells, and macrophages in the brains of JHMV infected mice. C57BL/6 WT or IFN-γR-/- mice were either mock infected or infected i.n. with 1×10^4 PFU WT virus. Whole brains were harvested at 5 dpi and IFNγ staining from each cell population was analyzed by flow cytometry. (A) The frequency of IFN-γ+ cells and (B) expression of IFN-γ (gMFI) for each cell type shown. Cell types analyzed were microglia (plum, circle), CD4+ T cells (magenta, square), CD8 T cells (bright pink, triangle), NK cells (carnation, diamond), DCs (pink, hexagon), and macrophages (purple, upside down triangle). Each point represents a mouse. The data in (A) is a pooled data from 3 independent studies while the data in (B) is from a representative experiment. Statistics were determined using a two-way ANOVA.